

# Geochemical Mobility Associated to Gold and Base Metal Occurrences of Mangodara Sector, in Southern Burkina Faso, Banfora Greenstone Belts (West African Craton)

Bernadin Gnamou\*, Hermann Ilboudo, Wilfried Antoine Bassou Toé, Sâga Sawadogo

Laboratoire Géosciences et Environnement (LaGE), Département des Sciences de la Terre, Ouagadougou, Burkina Faso

Email: \*bernadingnamou1610@gmail.com

---

**How to cite this paper:** Gnamou, B., Ilboudo, H., Toé, W.A.B. and Sawadogo, S. (2023) Geochemical Mobility Associated to Gold and Base Metal Occurrences of Mangodara Sector, in Southern Burkina Faso, Banfora Greenstone Belts (West African Craton). *Open Journal of Geology*, **13**, 1024-1053.

<https://doi.org/10.4236/oig.2023.1310044>

**Received:** July 28, 2023

**Accepted:** October 17, 2023

**Published:** October 20, 2023

Copyright © 2023 by author(s) and Scientific Research Publishing Inc.

This work is licensed under the Creative Commons Attribution International License (CC BY 4.0).

<http://creativecommons.org/licenses/by/4.0/>



Open Access

## Abstract

In the Mangodara area within the Banfora greenstone belts (Baoulé-Mossi domain of the West African Craton), our study focused on geochemical assessment of the mobility of major and trace elements. Gold and base metal occurrences are hosted in highly metamorphic felsic (metarhyolite) and intermediate (metadacite and metaandesite) formations. Common mineral assemblages made up of staurolite - kyanite - pyrophyllite are interpreted to represent the metamorphosed equivalent of aluminous hydrothermal alteration. Associated felsic and intermediate volcanic rocks are enriched in  $\text{Fe}_2\text{O}_3$ ,  $\text{K}_2\text{O}$  (metaandesite, metarhyolite) and depleted in  $\text{MgO}$ ,  $\text{Al}_2\text{O}_3$ ,  $\text{CaO}$ ,  $\text{P}_2\text{O}_5$ ,  $\text{Na}_2\text{O}$  (metarhyolite) and  $\text{Fe}_2\text{O}_3$ ,  $\text{MgO}$ ,  $\text{CaO}$  (metaandesite).  $\text{Al}_2\text{O}_3$  depletion in mineralized kyanite-staurolite bearing metarhyolites suggests corroded minerals. Mineralized metarhyolites show enrichment in Au, Ag, Ba, Bi, Cr, Cu, Eu, La, Mo, Ni, Pb, S, Sc, V and depletion in As, Sb, Co, Sn, Zn while mineralized metaandesites show enrichment in Au, Ag, As, Mo, S, Sb and depletion in Co, Sn, Zn, Bi, Cr, Cu, Eu, Ni, Pb, Sc, Ba, La, V are immobile in metaandesites. Finally, Ag, As, Sn appear as geochemical vectors for gold exploration in the study area since gold mineralization is characterized by Au + Ba + Cu + Eu + La + Mo + Ni + S association in metarhyolites and Au + S + Sb + As + Ag + Bi in metaandesites.

## Keywords

Geochemical Mobility, Aluminous Alteration, Metamorphism, Gold, Base Metal, Banfora Greenstone Belts, Mangodara

---

## 1. Introduction

The element mobility in hydrothermal fluids is documented in a variety of depo-

sits [1]-[6] and supported with experimental studies [7] [8]. The mobility is controlled by three main factors [9]: 1) the stability and composition of minerals in the unaltered rock, 2) the stability and composition of minerals in the altered product, and 3) the composition, temperature, and volume of the migratory fluid or melt phase. In addition, the undertaken studies on that phenomenon particularly in relation to alteration halos have significantly improved the understanding of geochemical elements mobility in aqueous systems. It is shown that acidic alteration produces a loss in Na-K in medium rare earth elements (MREE) such as Sm, Eu and Gd and a gain in Cu, As, Mo, Bi, Te and light rare earth elements (LREE), in particular La, Ce, Pr, Nd, Pm [10]. High field strength elements (HFSE), and rare earth elements (REE) are generally considered to be immobile during secondary processes, opposite of large ion lithophile elements (LILE) which are mobile [11] [12]. Using the constant ratios of La/Th and La/Sc observed in shales [13] estimated the upper crustal thorium and scandium contents at 11 ppm and 10.7 ppm, respectively. Recent studies combining whole-rock and mineral chemistry in volcanogenic massive sulphides (VMS) deposits, showed that LREE (La to Sm) and Eu are mobile in the alteration halo of Brace-mac-McLeod deposits [2]. In the West African Craton (WAC) (**Figure 1(a)**), the Baoulé-Mossi domain of the Léo/Man shield hosts gold and base metal occurrences [14]-[22]. Likely, in the metallogenic province of the WAC, alterations are almost systematically associated with metals descriptions [17] [20] [23] [24] [25] [26] [27], but the geochemical signatures attributable to metal content, in opposite, is little or no assessed. The present study deals with geochemical data from a gold and base metal occurrence in the southern Banfora belts, close to the Ivory Coast border. The occurrences are associated with silico-aluminous kyanite, staurolite, garnet, Fe ± Mg muscovite paragenetic assemblage typical of amphibolite metamorphism facies [23], but there is no information on the geochemical features of host rock. In this paper, we discuss the relationship between the mobility of geochemical elements in order to contribute to increasing the chance for exploration in this part of the Birimian system, since the use of geochemistry in mineral exploration is invaluable, particularly in relation to the understanding of alteration, mineralization-related processes, and guide for exploration.

## 2. Geological Setting

Several studies [16] [28] [29] [30] [31] present the geological configuration of the Léo/Man shield in two domains, respectively the western Kénéma-Man domain > 2500 Ma and the eastern Baoulé-Mossi domain dated at ~2000 Ma [28] [31]. The Baoulé-Mossi domain consists mainly of volcanic and sedimentary belts and granitoid intrusions [18] [30] [32]-[41]. Burkina Faso which extends on the Baoulé-Mossi domain is composed of Paleoproterozoic basement greenstone belts and granitoid (80%) covered in its western, northern and eastern margin by Neoproterozoic to Cambro-Ordovician sedimentary (1000 - 435 Ma) formations (20%). The belts are essentially made up of metavolcanic rocks, ranging

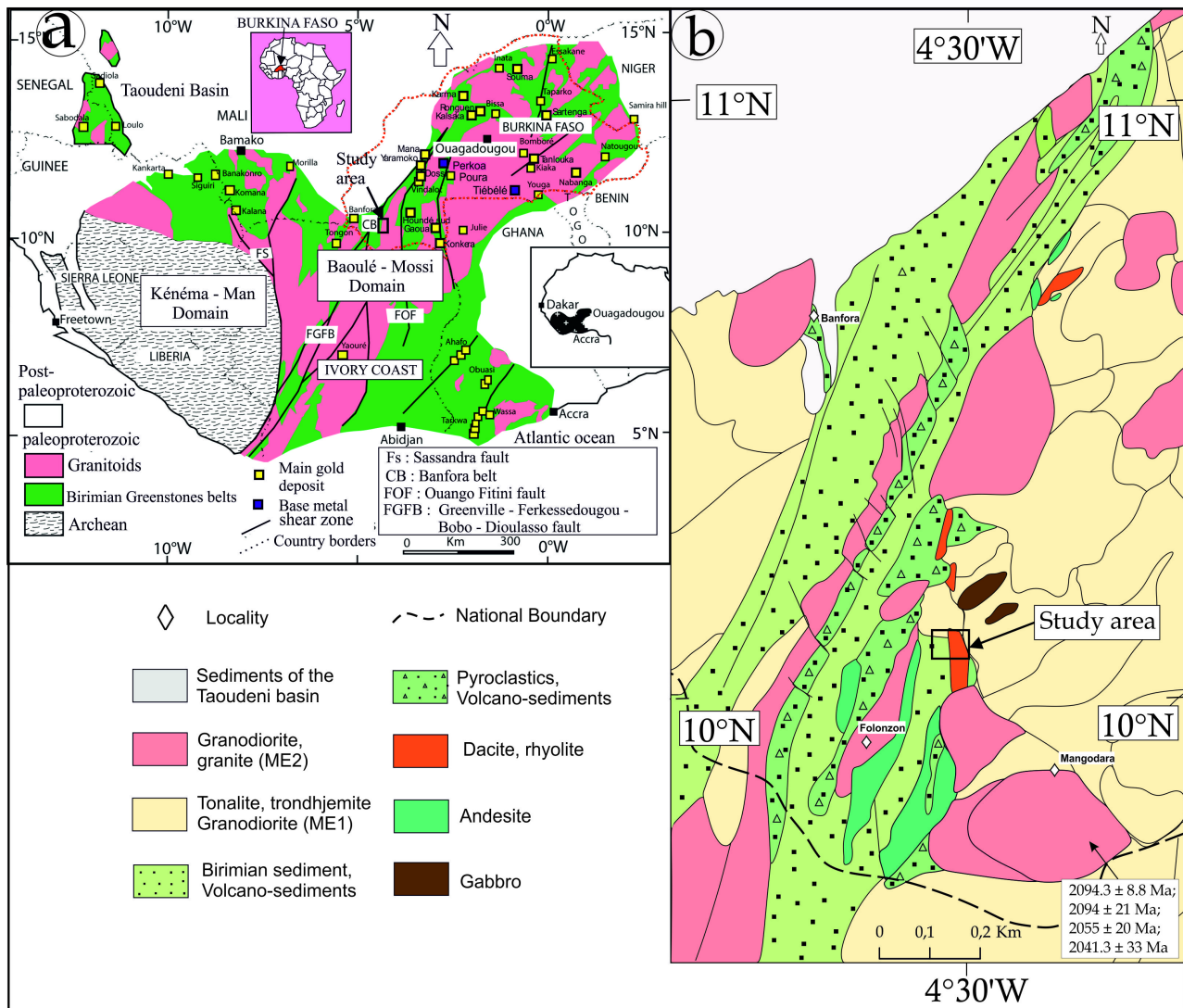


**Figure 1.** (a) geological map of the Leo/Man shield and the most important gold deposits across the WAC (Modified from [17]); (b) simplified geological map of Banfora green belt (modified from [34]) and location of the studied area.

from metabasalts to metarhyolites and metasedimentary rocks including quartzites and metapelites [23] [36] [42] [43]. Specifically, the Banfora belt that extends over 160 km long and 35 km wide [43] in Burkina Faso lays up to Côte d'Ivoire; and is intersected by the Bobo-Dioulasso high strain corridor representing the continuity of the major Greenville-Ferkéssédougou-Bobo-Dioulasso shear zone (**Figure 1(b)**). The eastern part of the Banfora belt consists of interlayered units of basalts, andesites, volcano-sediments and rhyolites, 2 to 4 km thick, while the western part is composed solely of volcano-sediments according to [36]. The global stratigraphy of the belt proposed by these authors and revised by Ilboudo [43] suggests, from bottom to top: 1) deposition of ultramafic rock; 2) mafic volcanic; 3) subsequent deposition of lava flow and projection (pyroclastite and lapilli tuff); 4) deposition of siliceous rock (exhalite); 5) emplacement of pelitic and turbiditic sediments; 6) emplacement of the pre-collision eastern granite

and 7) emplacement of the post-collision western granite. The volcanic activity that prevailed in West Burkina Faso took place between 2190 Ma and 2160 Ma (Eoeburnean) according to [36] and presents a juvenile character with regard to  $\varepsilon$ Hf (~0 to +8) [38]. The exhalites constitute the upper horizon of the lithostratigraphy of the volcanic formations of the eastern part of the belt and subvolcanic rocks consist mainly of porphyry microdiorite, dolerite sills and dykes [43]. Syn-tectonic intrusions (granite and granodiorite) emplaced in the favor of Greenville- Ferkéssédougou-Bobo-Dioulasso regional shear zone known from Liberia and Ivory Coast [36] [43] [44]. Based on geochemical and geotectonic settings, [43] pointed out that granitoids in western and eastern margins of the Banfora belt are respectively post- and pre-collisional. Geochemically, granitoid intrusions show arc volcanic in character, including negative Ta, Nb and Sr anomalies and mostly older than 2100 Ma [38]. In nearby areas, pegmatite associated with granitoids and migmatitic gneiss potentially contains rare metals [40] [41]. The study area consists of a set of dominantly metamorphosed volcanic metaformations (metarhyolite, rhyolitic tuff, metadacite, metaandesite, metabasalt (**Figure 2(a)**) and **Figure 2(b)**). Rare outcrops of sulphidic felsic and

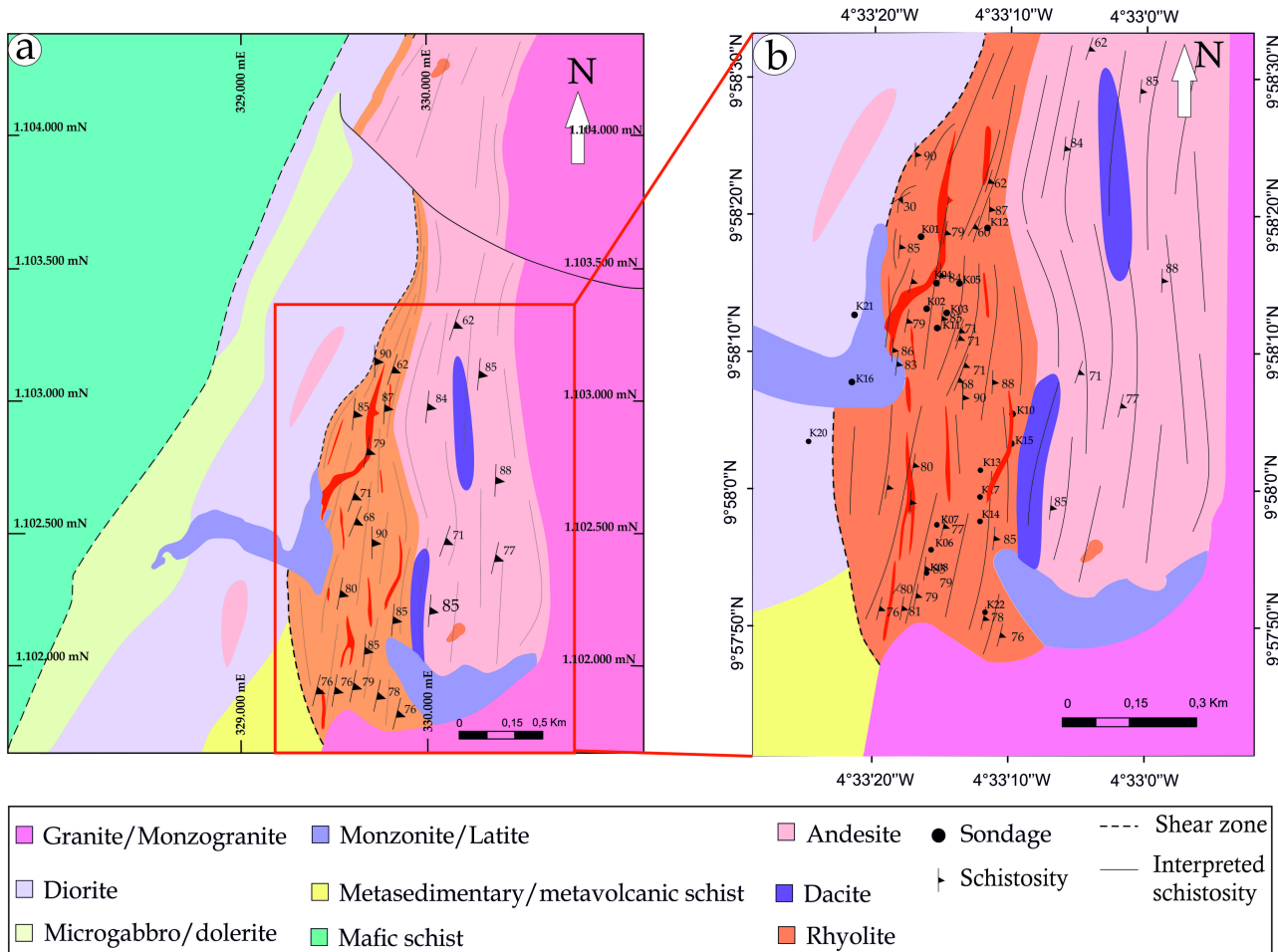


**Figure 2.** Geology environment. (a) regional geology; (b) geological map of the study area.

highly siliceous formations (metarhyolite, cherts and quartzites) that have resisted the weathering appear as main host rocks [23]. Late monzonite, granodiorite, and diorite cross-cut the entire volcanic package. The occurrences are hosted by a narrow northeast–southwest trending shear zone.

### 3. Methodology

#### 3.1. Sampling

The fieldwork consisted of describing and sampling several diamond drill holes for further investigations. The samples come from two drill holes (K7 and K15), following a good spatial coverage of the alteration zones. A total of twenty rock samples from these drill holes have been collected. The sampling was undertaken on the different lithologies, including all styles of mineralization and alteration following two-meter spacing. Fifty thin sections were made including twenty at Western Australia University and thirty at Université Joseph KI-ZERBO at the Laboratoire Geosciences et Environment (LaGE). Detail investigation is operated under a Nikon Eclipse 50i POL type polarizing microscope (transmitted and reflected lights), coupled to a camera. We use acronyms for rock-forming mineral in [45]. GDCKit of [46] was used for much of the ternary plotting.

#### 3.2. Analytical Method

Part of this study is based on whole-rock geochemical data from the drill cores. Samples were analyzed by XRF diffraction for major elements and rare earth and trace elements by Inductively Coupled Plasma Mass Spectrometry (ICP-MS) at the ACME Laboratory in Vancouver. Twenty of the analyzed samples from metarhyolites, metadacites and metaandasites, were used in this paper (**Table 1**). Samples were crushed and pulverized to 200 mesh and sample fragments (0.2 g) were placed in graphite crucibles and with lithium borate flux added. The crucibles were placed in an oven and heated at 1025°C for 25 min. Each melted sample was then dissolved in 5% HNO<sub>3</sub>. A blank and internal standard (STD SO-15 reference material) were carried through the weighing, digestion and analysis stages to check for accuracy. Calibration standards, verification standards and reagent blanks were also added to the sample sequence for testing. To examine the geochemical characteristics of the mineralization, principal component analysis (PCA) was performed on whole-rock geochemical data in order to discriminate elements associated with gold mineralization from those that are not related to the process. For the exercise, REE (La, Eu) LILE (Ba, Cu, Pb), HFSE (Sc), metals (Au, Co, Mo, V, Ag, Sb, Sn, Cr, Ni, As, Zn, Bi) and S were used. To address the closure problem in multivariate statistical analysis of compositional datasets, we applied a centered log-ratio (CLR) transformation [47] to the elemental data prior to principal component analysis (PCA). We applied to extract only principal components (PC) with eigenvalues greater than 1. The extracted Principal Components (PC) were orthogonally rotated by the Varimax method [48] to maximize the variability between all input variables and, facilitate

**Table 1.** Lithogeochemical data for the Mangodara area.

Sample	K7_47	K7_151	K7_163	K7_184	K7_187	K15_393	K7_76	K15_280	K15_323	K7_95	K7_127
Element/ Oxyde	Rhyolite	Rhyolite	Rhyolite	Rhyolite	Rhyolite	Rhyolite	Dacite	Dacite	Dacite	Andesite	Andesite
SiO <sub>2</sub> (%)	64.94	60.81	67.16	71.89	70.63	65.35	70.50	64.96	63.40	68.49	66.97
Al <sub>2</sub> O <sub>3</sub>	14.70	7.10	15.34	15.37	8.27	15.10	14.82	14.40	14.56	12.24	16.90
Fe <sub>2</sub> O <sub>3</sub>	6.72	11.51	7.65	3.96	6.65	7.58	4.88	6.31	7.12	5.52	7.42
FeO	6.05	10.36	6.88	3.56	5.98	6.82	4.39	5.67	6.41	4.97	6.68
MgO	3.23	0.06	0.18	0.31	0.26	2.40	1.72	2.42	3.92	3.53	0.32
Na <sub>2</sub> O	0.33	0.30	0.65	0.83	0.18	0.31	0.35	0.21	0.14	0.19	0.70
K <sub>2</sub> O	0.92	0.95	3.73	2.55	1.29	0.78	0.73	3.32	2.10	0.81	2.87
CaO	2.62	0.46	0.35	1.17	0.51	2.62	2.17	2.09	4.69	5.08	0.80
TiO <sub>2</sub>	0.16	0.12	0.18	0.20	0.24	0.19	0.35	0.30	0.34	0.45	0.72
P <sub>2</sub> O <sub>5</sub>	1.39	0.61	0.39	0.73	0.93	1.56	1.27	1.45	1.36	1.02	1.34
MnO	0.07	0.01	0.01	0.01	0.02	0.11	0.08	0.09	0.11	0.13	0.03
LOI	4.52	16.70	5.52	4.02	11.02	5.15	3.51	4.71	3.01	3.11	2.65
<b>Sum</b>	<b>98.94</b>	<b>97.48</b>	<b>100.40</b>	<b>100.65</b>	<b>99.34</b>	<b>100.39</b>	<b>99.89</b>	<b>99.63</b>	<b>100.04</b>	<b>100.01</b>	<b>100.00</b>
Au	0.05	7.45	0.03	0.06	0.08	0.06	0.06	0.05	0.08	0.04	0.62
Ag	0.25	0.25	1.10	0.25	0.25	0.25	0.25	0.25	0.25	0.25	0.25
As	105.90	139.10	19.70	10.50	150.00	73.40	2529.60	49.80	20.10	25.50	45.90
Ba	544.40	1907.00	976.40	901.30	411.10	301.80	303.90	687.30	526.80	377.90	906.20
Be	0.89	0.48	0.71	0.95	0.42	1.05	0.84	0.80	0.89	0.77	0.55
Bi	0.11	0.15	0.17	0.04	0.26	0.04	0.04	0.10	0.06	0.08	0.09
Cd	0.14	0.53	0.26	0.14	0.12	0.08	0.08	0.08	0.06	0.07	0.13
Co	22.60	20.90	33.60	14.00	26.00	23.60	16.30	23.10	23.00	15.70	32.50
Cr	100.00	114.00	133.00	83.00	78.00	85.00	121.00	81.00	86.00	121.00	138.00
Cs	1.46	1.52	3.12	2.42	2.53	1.18	0.95	3.74	2.88	2.48	6.01
Cu	44.00	88.00	53.00	31.00	70.00	95.00	23.00	45.00	44.00	12.00	38.00
Ga	16.86	15.59	18.34	16.91	12.53	16.97	16.54	16.56	16.42	13.32	18.38
Ge	0.63	0.28	0.91	1.40	0.37	0.91	0.74	0.63	0.85	0.54	1.00
Hf	3.54	5.16	3.85	3.66	3.58	3.34	3.73	3.10	3.02	2.97	4.41
In	0.03	0.04	0.03	0.03	0.02	0.03	0.02	0.04	0.03	0.04	0.03
Li	86.80	13.20	13.40	40.00	20.90	85.00	86.80	20.70	19.50	12.90	28.10
Mo	0.80	3.50	1.70	1.60	2.10	1.30	1.70	1.80	1.20	1.70	6.70
Nb	1.94	1.48	1.86	1.99	2.83	2.48	5.58	2.59	2.69	5.16	9.33
Ni	37.00	78.00	51.00	31.00	36.00	40.00	33.00	30.00	34.00	33.00	41.00

**Continued**

Pb	7.40	27.00	31.40	20.20	5.90	4.50	9.10	10.00	6.20	7.90	17.70
Rb	28.71	21.18	90.23	71.38	35.41	17.43	19.30	86.79	57.61	28.12	71.01
S	2.65	5.24	3.11	1.33	3.55	2.46	0.78	2.11	1.43	0.70	1.91
Sb	6.32	4.56	3.54	4.58	7.53	8.90	6.56	4.42	3.44	5.83	5.23
Sc	18.90	21.80	20.10	20.10	16.40	20.60	11.50	19.50	20.80	16.40	20.20
Se	12.70	3.00	0.60	0.70	6.70	0.60	2.10	2.00	0.90	2.50	0.25
Sn	1.40	0.90	1.10	1.30	0.80	0.60	1.60	1.50	1.20	1.30	2.00
Sr	142.78	144.33	122.71	171.07	145.51	130.20	139.76	105.98	149.55	132.98	245.22
Ta	0.30	0.16	0.28	0.28	0.21	0.30	0.64	0.33	0.34	0.55	0.82
Te	0.03	0.03	0.05	0.03	0.15	0.03	0.12	0.12	0.13	0.03	0.03
Th	4.86	5.85	5.11	5.61	4.32	4.09	6.26	4.51	4.44	4.15	5.43
Tl	0.83	13.63	5.18	1.29	1.70	0.69	0.77	1.22	0.81	0.84	11.25
U	1.44	2.73	1.63	1.78	1.42	1.40	2.25	1.51	1.46	1.54	2.31
V	116.00	101.00	146.00	117.00	106.00	138.00	80.00	141.00	134.00	97.00	139.00
W	0.20	1.80	0.40	0.60	0.90	0.90	0.90	0.50	0.20	0.50	3.30
Y	21.60	12.26	9.26	17.78	10.90	18.32	8.49	18.16	20.37	18.98	16.37
Zn	127.00	93.00	18.00	29.00	14.00	112.00	51.00	61.00	97.00	75.00	47.00
Zr	129.50	199.50	149.00	144.30	136.10	124.10	142.60	114.20	114.90	105.20	171.90
<b>REE</b>											
La	23.80	41.14	25.62	28.72	23.90	21.39	24.75	22.67	22.26	20.38	28.27
Ce	51.31	83.35	55.48	61.32	51.04	46.20	51.06	49.25	48.02	43.98	60.66
Pr	5.94	9.68	6.22	7.01	6.04	5.29	5.49	5.59	5.58	5.06	7.11
Nd	22.20	35.43	22.74	25.42	22.29	19.68	18.95	20.77	20.26	18.50	26.02
Sm	4.39	6.11	4.36	4.89	4.33	3.98	3.43	3.87	4.01	3.76	5.03
Eu	1.14	1.57	1.00	1.20	1.03	0.97	0.85	0.96	1.05	0.96	1.08
Gd	3.99	4.44	3.52	4.17	3.60	3.52	2.71	3.71	3.75	3.47	4.07
Tb	0.63	0.56	0.43	0.65	0.49	0.56	0.38	0.56	0.58	0.52	0.60
Dy	4.09	2.88	2.08	3.73	2.58	3.53	2.01	3.56	3.62	3.52	3.36
Ho	0.84	0.51	0.39	0.72	0.45	0.73	0.34	0.72	0.77	0.72	0.67
Er	2.49	1.42	1.08	1.97	1.29	2.21	1.58	2.16	2.27	2.23	1.78
Tm	0.39	0.22	0.18	0.29	0.20	0.35	0.14	0.33	0.33	0.34	0.26
Yb	2.29	1.52	1.25	1.83	1.31	2.19	0.88	2.05	2.28	2.19	1.74
Lu	0.35	0.25	0.21	0.26	0.20	0.34	0.14	0.31	0.31	0.31	0.25

Sample	K7_198	K7_202,86	K7_203	K15_52	K15_85	K15_131	K15_217	K15_257	K15_359
Element/Oxyde	Andesite	Andesite	Andesite	Andesite	Andesite	Andesite	Andesite	Andesite	Andesite
SiO <sub>2</sub> (%)	73.54	65.84	63.12	63.70	61.92	62.99	69.45	62.69	64.45
Al <sub>2</sub> O <sub>3</sub>	13.71	15.25	15.69	14.44	14.23	13.64	11.35	14.15	15.81
Fe <sub>2</sub> O <sub>3</sub>	3.85	6.05	7.51	6.69	6.78	6.91	6.51	7.64	7.42
FeO	3.46	5.44	6.76	6.02	6.10	6.21	5.85	6.87	6.68
MgO	0.73	1.45	1.74	3.44	3.47	3.42	0.43	3.31	3.20
Na <sub>2</sub> O	0.36	1.20	1.61	0.65	2.71	2.96	0.35	0.22	0.23
K <sub>2</sub> O	2.51	2.11	1.79	2.33	2.32	1.61	2.69	2.66	0.65
CaO	1.65	5.65	6.24	6.33	6.08	5.49	0.38	4.40	2.64
TiO <sub>2</sub>	0.58	0.64	0.65	0.46	0.66	0.65	0.50	0.52	0.45
P <sub>2</sub> O <sub>5</sub>	0.55	1.51	1.50	1.40	1.38	1.38	1.19	1.43	1.47
MnO	0.05	0.13	0.15	0.12	0.12	0.12	0.02	0.12	0.13
LOI	2.65	1.65	1.05	1.05	1.99	1.89	7.11	4.13	4.03
<b>Sum</b>	<b>99.79</b>	<b>100.88</b>	<b>100.30</b>	<b>99.93</b>	<b>100.98</b>	<b>100.36</b>	<b>99.34</b>	<b>100.52</b>	<b>99.73</b>
Au	0.04	0.00	0.08	0.04	0.02	0.00	1.92	0.04	0.08
Ag	0.25	0.11	0.25	0.25	0.25	0.25	1.60	0.25	0.25
As	10.30	9.60	13.00	6.70	11.70	12.20	3987.20	76.10	158.10
Ba	770.50	742.80	697.50	663.70	927.30	721.20	856.90	561.70	266.40
Be	0.88	1.46	1.35	0.91	0.85	0.87	0.82	0.99	1.10
Bi	0.02	0.03	0.03	0.09	0.08	0.11	0.46	0.26	0.11
Cd	0.05	0.15	0.24	0.14	0.22	0.14	0.05	0.09	0.08
Co	27.10	18.60	23.70	24.40	21.10	21.70	19.60	22.30	23.80
Cr	130.00	91.00	100.00	56.00	73.00	77.00	101.00	82.00	99.00
Cs	2.09	6.11	4.46	2.22	4.03	3.38	5.03	4.02	0.86
Cu	20.00	45.00	56.00	47.00	47.00	48.00	35.00	58.00	17.00
Ga	14.87	17.42	17.68	16.30	16.37	16.03	14.80	16.02	17.13
Ge	1.27	1.23	1.08	0.76	0.86	0.81	0.37	0.58	1.20
Hf	2.82	2.73	3.04	2.91	3.48	3.35	2.91	3.45	3.53
In	0.03	0.05	0.06	0.04	0.05	0.04	0.03	0.03	0.02
Li	33.40	14.00	14.70	20.10	24.30	28.00	23.90	41.00	90.00
Mo	1.80	2.30	1.50	1.40	1.20	1.60	2.00	2.10	0.80
Nb	8.85	9.56	9.89	2.38	9.15	6.82	4.17	4.56	3.61
Ni	62.00	27.00	37.00	26.00	23.00	25.00	31.00	31.00	29.00
Pb	12.70	20.60	20.90	7.30	13.20	9.10	9.00	8.40	6.60
Rb	67.60	72.66	60.52	60.67	70.54	43.41	92.64	77.86	14.93

Sample	K7_198	K7_202.86	K7_203	K15_52	K15_85	K15_131	K15_217	K15_257	K15_359
Element/Oxyde	Andesite	Andesite	Andesite	Andesite	Andesite	Andesite	Andesite	Andesite	Andesite
S	0.38	0.11	0.28	1.04	0.41	0.89	3.57	2.11	2.05
Sb	4.18	4.08	4.90	4.11	4.52	4.42	25.47	4.50	6.98
Sc	19.90	19.40	19.50	21.00	20.90	19.50	18.10	20.40	21.40
Se	0.25	0.25	0.25	1.50	0.60	1.00	4.60	2.60	0.25
Sn	1.50	1.90	2.20	1.70	1.90	1.80	1.80	1.20	0.80
Sr	121.98	244.67	258.17	164.16	193.42	182.34	251.04	97.77	116.14
Ta	0.71	0.72	0.85	0.26	0.61	0.64	0.38	0.47	0.49
Te	0.03	0.03	0.06	0.08	0.03	0.12	0.49	0.21	0.03
Th	4.57	4.92	5.42	4.65	4.37	4.35	5.26	4.58	4.81
Tl	1.10	0.96	0.75	0.62	0.69	0.50	2.70	1.28	0.42
U	1.31	0.71	0.87	1.48	1.47	1.47	1.62	1.57	1.23
V	115.00	121.00	126.00	136.00	134.00	133.00	111.00	128.00	136.00
W	1.00	0.70	0.40	0.05	0.40	0.60	1.20	0.50	0.60
Y	19.93	23.16	24.78	22.17	22.24	21.31	9.03	23.26	19.52
Zn	73.00	80.00	102.00	60.00	67.00	69.00	10.00	63.00	113.00
Zr	104.90	109.60	102.10	115.70	118.90	142.20	125.10	130.40	133.00
<b>REE</b>									
La	23.01	27.12	26.87	23.43	22.33	22.02	25.48	23.44	24.05
Ce	50.04	53.34	56.52	50.25	48.40	47.46	55.42	51.06	51.57
Pr	5.82	6.39	6.59	5.83	5.55	5.49	6.37	5.87	5.91
Nd	21.35	23.45	23.96	21.89	20.43	20.42	23.60	21.78	21.83
Sm	4.17	4.30	4.60	4.27	4.19	4.00	4.52	4.42	4.34
Eu	0.96	1.11	1.22	1.05	1.02	1.03	1.00	1.19	1.27
Gd	3.95	4.02	4.25	3.95	3.86	3.76	3.43	4.03	3.90
Tb	0.60	0.64	0.64	0.63	0.58	0.60	0.46	0.65	0.63
Dy	3.85	4.05	4.22	3.94	3.97	3.90	2.33	4.19	3.82
Ho	0.79	0.87	0.89	0.83	0.84	0.84	0.38	0.90	0.77
Er	2.44	2.52	2.75	2.49	2.51	2.48	0.94	2.64	2.23
Tm	0.38	0.39	0.43	0.39	0.39	0.38	0.14	0.39	0.32
Yb	2.41	2.56	2.64	2.51	2.35	2.42	0.98	2.48	2.06
Lu	0.37	0.38	0.38	0.35	0.32	0.35	0.15	0.36	0.31

the interpretation of loading factors.

## 4. Results

### 4.1. Petrography and Mineralogy

Three main types of metamorphosed volcanic rocks were identified during petro-

graphic examination. They correspond to rhyolitic, dacitic and andesitic composition. Metarhyolites show grano-lepidoblastic and locally porphyroblastic texture including kyanite 2 - 5 mm, staurolite 1 - 2 mm and garnet 1 - 2 mm that are overprinted by lepidoblastic texture with dominant mica content. They are made up of quartz phenocrysts (5 - 10 vol.%), 1 - 2 mm in diameter rounded and corroded (**Figure 3(a)**) within siliceous microcrystalline matrix (70 vol.%). The matrix consists of recrystallized quartz, sericite and chlorite flakes. Metadacites develop granolepidoblastic and locally porphyritic texture including plagioclase of 2 - 3 mm in size. Common mineral association is quartz (1 - 5 vol.%), plagioclase (15 - 20 vol.%) up to 1 - 3 mm, deformed and altered into sericite (**Figure 3(b)**), while biotite (2 - 10 vol.%) is replaced by chlorite. Metaandesites show granolepidoblastic texture consisting of plagioclase (20 - 30 vol.%) (**Figure 3(c)**), biotite (10 - 20 vol.%), quartz (10 - 15 vol.%) and hornblende (5 - 10 vol.%) (**Figure 3(d)**).

The metamorphic minerals are mainly kyanite, staurotide, garnet, chloritoid, hornblende and biotite (**Figure 4(a)**, **Figure 4(b)** and **Figure 4(d)**). In places, the kyanite and staurotide are corroded and altered to sericite (**Figure 4(c)**) in a low degree of metamorphism. Strong hydrothermal alteration includes pyrite and pyrrhotite-rich in association with sericite and quartz. Therefore, association

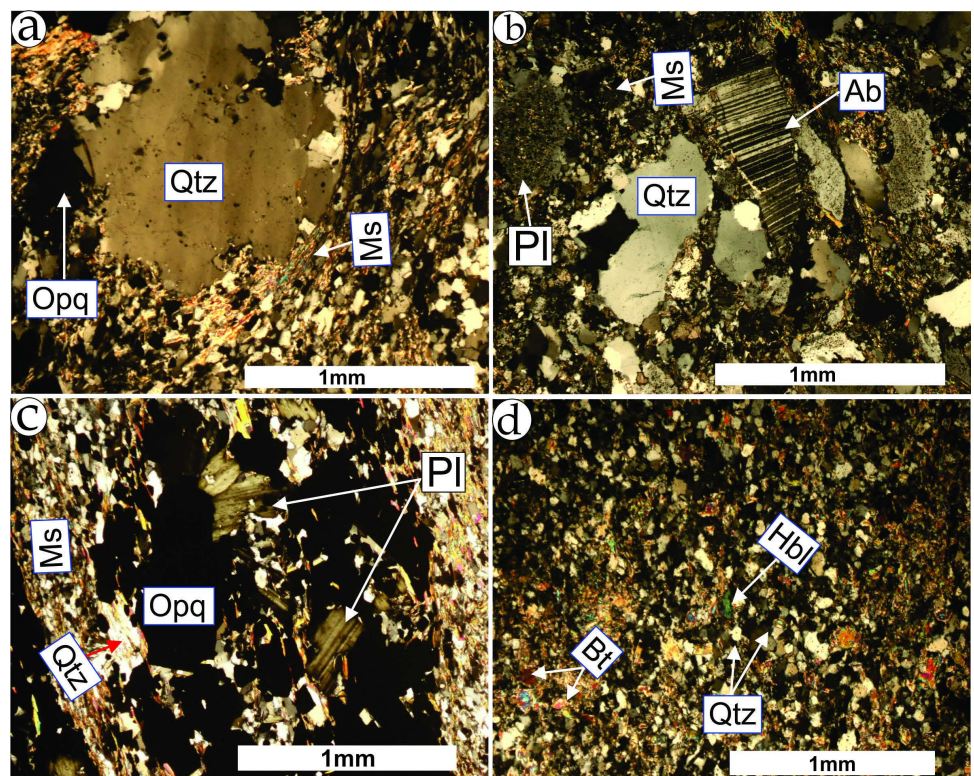


**Figure 3.** Microscopic detail of mineral assemblages observed in various lithologies. (a) Primary corroded quartz in metarhyolites; (b) Plagioclase phenocrysts in a siliceous quartz matrix associated with sericite flakes in metadacites; (c) Plagioclase phenocrysts in association with opaques in metaandesites; (d) Quartz-biotite-hornblende matrix in metaandesites. Qtz: Quartz; Ms: Muscovite; Opq: Opaque; Pl: Plagioclase; Ab: Albite; Bt: Biotite; Hbl: Hornblende.

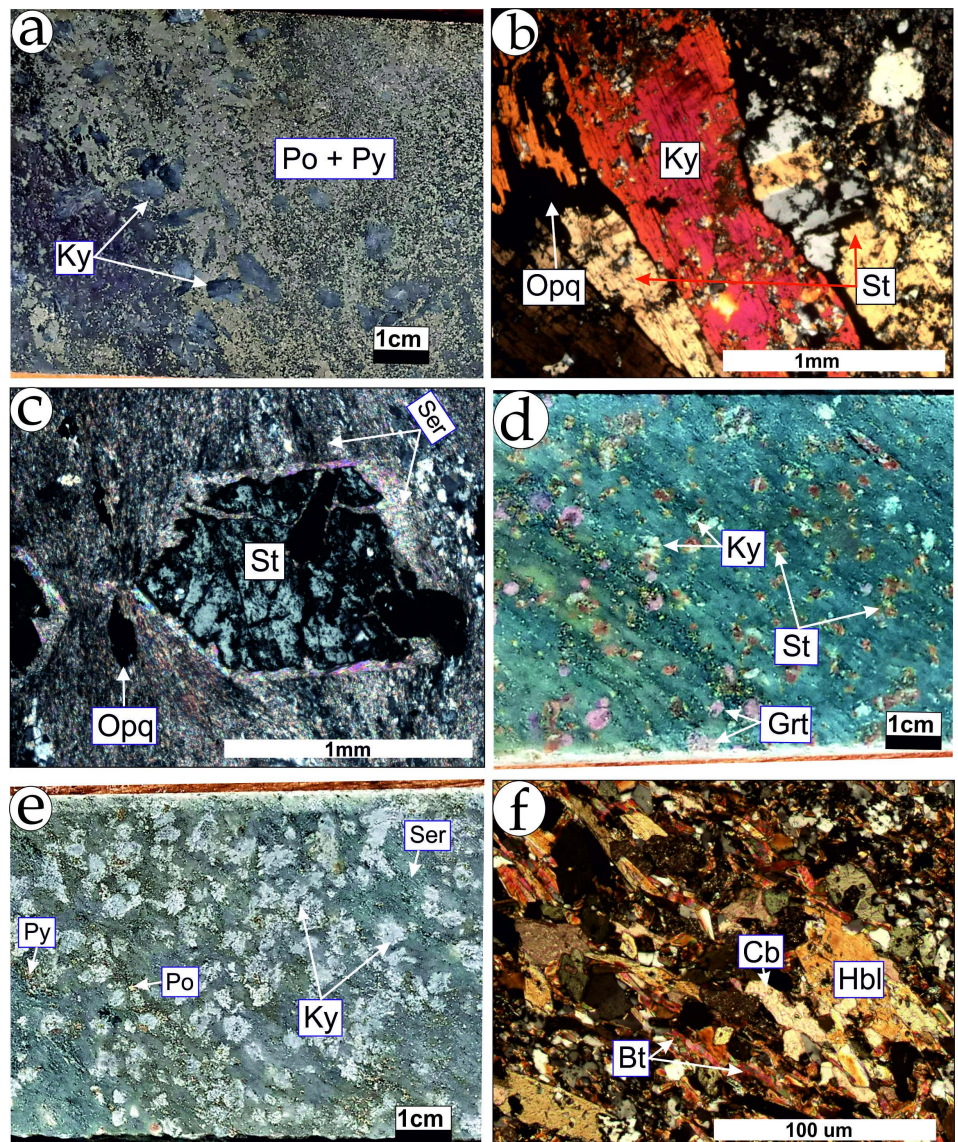


**Figure 4.** Macroscopic views of metamorphic minerals: a) semi-massive pyrrhotite associated with kyanite; b) Kyanite-staurolite porphyroblast association in metarhyolites; c) Corroded staurolite; d) Kyanite - staurolite - garnet paragenetic association; e) Kyanite porphyroblast in the metarhyolites; f) Carbonate, hornblende and biotite association in metaandesites. Ky: Kyanite; St: Staurolite; Qtz: Quartz; Ser: Sericite; Grt: Garnet; Py: Pyrite; Po: Pyrrhotite; Hbl: Hornblende; Opq: Opaque; Cb: Carbonate.

pyrite-pyrrhotite-kyanite is noticeable in rhyolite (**Figure 4(e)**). Hydrothermal alteration is also noted within monomictic breccia supported by clasts, showing angular and puzzle-shaped blocky textures implying chlorite and sericite. These later minerals appear in dacite where sericite develops flakes and quartz, recrystallized sub-grained. Carbonate is specific in andesite (**Figure 4(f)**).

## 4.2. Geochemical Data

### 4.2.1. Majors and Traces Data

Rocks are classified using the Nb/Y vs Zr/Ti binary plot of [49] (**Figure 5**). The

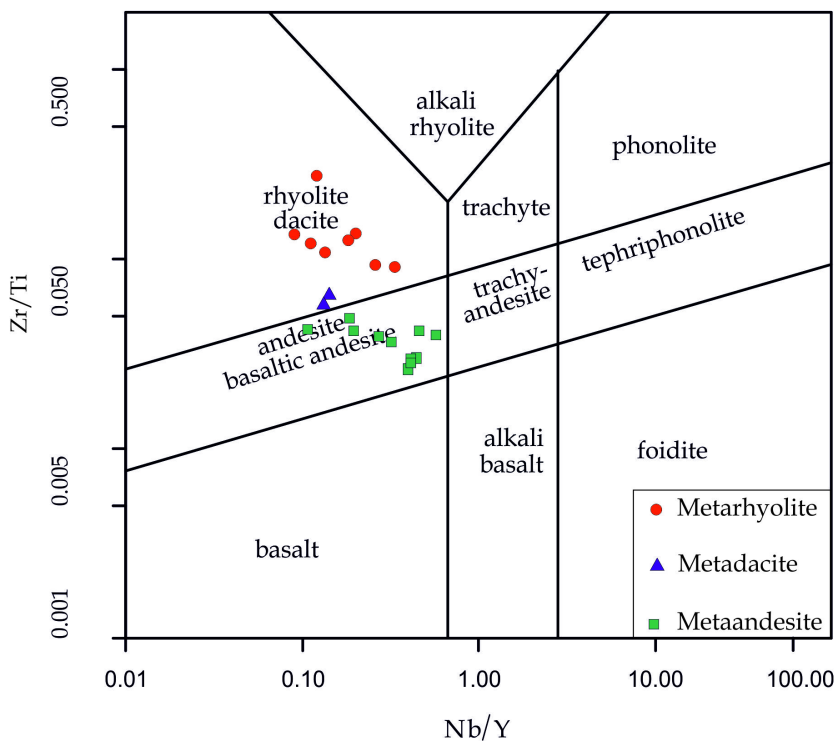


**Figure 5.** Diagram of classification of different volcanic rocks. Nb/Y Vs Zr/Ti diagram [46].

Nb/Y vs Zr/Ti diagram confirms the lithology made up of rhyolite, dacite and andesite composition. However, one metadacite sample is located in the andesite field. This shows that a sample of metadacite is enriched in titaniferous oxide.

#### 4.2.2. Geochemical Behavior of Rocks Mineral Component in A'CF and A'KF Ternary Plots

In the AFM, A'CF and A'KF ternary diagrams (Figure 6) established by [50] [51], the altered felsic and intermediate volcanic rocks show three trends: We calculated the number of moles of the components, by dividing the percentages by weight of oxides by the molecular masses (Table 2). 1) The samples from mineralized metarhyolite with high Fe plotted in the AFM and A'CF ternary diagram suggests the presence of chloritoids, but they are randomly distributed in the A'KF ternary diagram; 2) Two samples of unmineralized metarhyolite with high Mg plotted in the AFM and A'CF ternary diagram suggest the presence of chlorite but are randomly distributed in the A'KF ternary diagram between chlorite alteration trend and sericite alteration trend; 3) Two samples from metadacite with high Mg and K plotted in the AFM suggest the presence of chlorite and sericite, with high Fe, Mg, Ca content plot in A'CF diagram describe the presence of chloritoid, carbonates and hornblendes while they are scarcely reported in the A'KF diagram either describing biotite alteration or the presence of chloritoid; 4) Samples from mineralized metaandesite with high Fe, Mg, Ca plotted in the AFM and A'CF ternary diagram suggest the presence of chlorite,

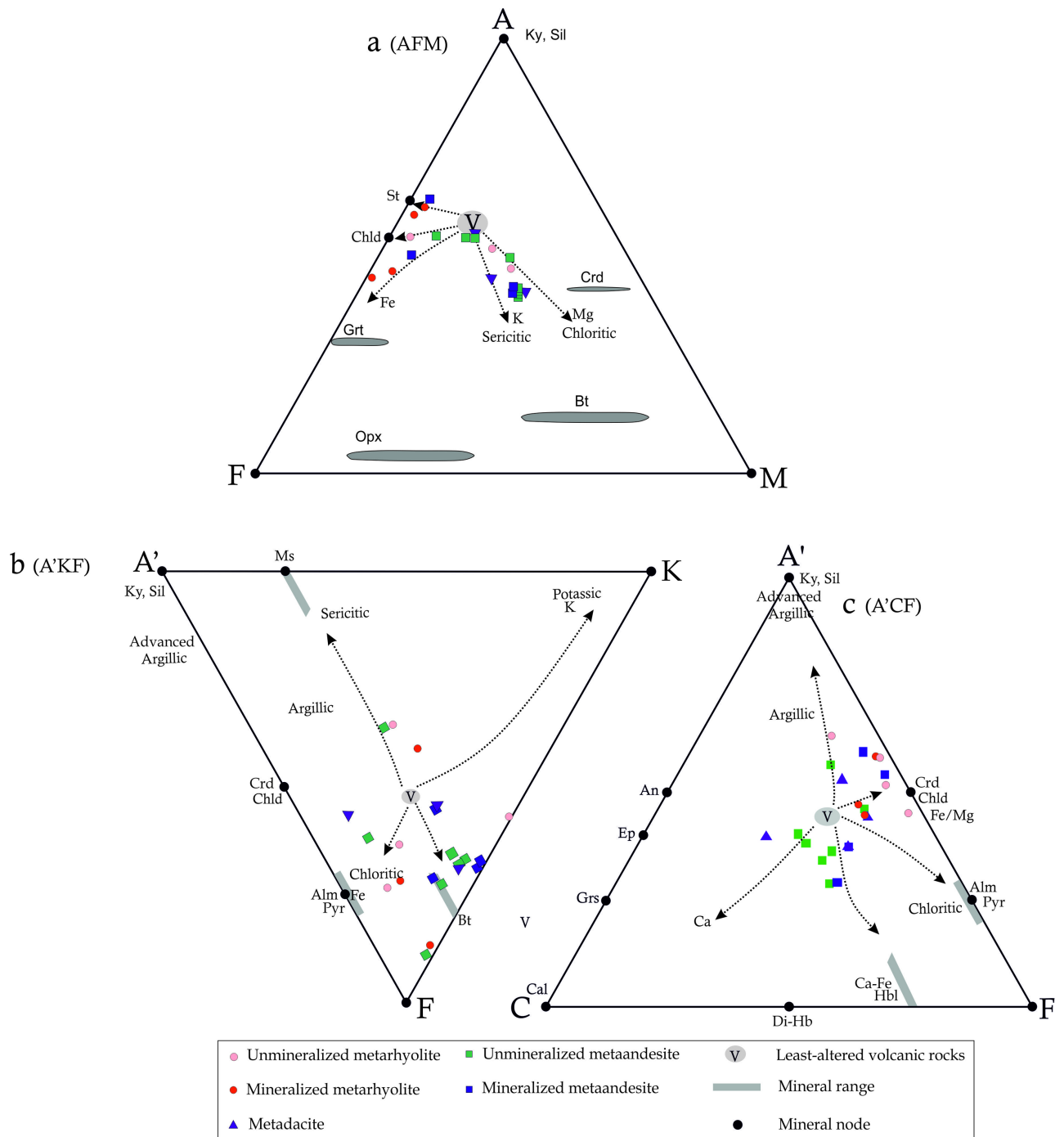


**Figure 6.** Ternary diagrams in the AFM, A'FK and A'CF systems. A'CF.  $A' = \text{Al}_2\text{O}_3 + \text{Fe}_2\text{O}_3 - (\text{K}_2\text{O} + \text{Na}_2\text{O})$ ,  $C = \text{CaO}$ ,  $F = \text{FeO} + \text{MnO} + \text{MgO}$ . A'FK.  $A' = \text{Al}_2\text{O}_3 + \text{Fe}_2\text{O}_3 - (\text{K}_2\text{O} + \text{Na}_2\text{O} + \text{CaO})$ ,  $K = \text{K}_2\text{O}$ ,  $F = \text{FeO} + \text{MnO} + \text{MgO}$ . AFM.  $A = \text{Al}_2\text{O}_3 - \text{K}_2\text{O}$ ;  $F = \text{FeO}$ ,  $M = \text{MgO}$ .

sericite, chloritoids, staurolite and hornblendes but records high Fe value in the A'FK diagram suggesting biotite alteration; 5) The samples from unmineralized metaandesite with high Fe, Mg, Ca plots in ACF and A'CF ternary diagram respectively describe the presence of chlorite, sericite, chloritoid, hornblende and carbonate whereas they show six samples enriched in iron in the A'FK diagram

**Table 2.** AFM, A'CF and A'KF coordinates for rocks in the Mangodara area.

Sample	K7_47	K7_151	K7_163	K7_184	K7_187	K15_393	K7_76	K15_280	K15_323	K7_95	K7_127
Element/%	Rhyolite	Rhyolite	Rhyolite	Rhyolite	Rhyolite	Rhyolite	Dacite	Dacite	Dacite	Andesite	Andesite
<b>AFM</b>											
A	44.93	29.06	52.50	68.36	42.90	47.45	56.97	43.16	39.17	41.43	57.26
F	24.08	35.15	34.16	39.82	45.86	24.46	29.82	29.37	23.43	26.81	30.50
M	26.99	0.71	2.14	4.26	4.17	20.37	17.79	24.69	31.87	32.89	3.44
<b>A'CF</b>											
A'	44.59	45.17	58.16	63.29	51.70	47.28	53.04	44.35	37.38	36.37	59.54
C	12.21	2.95	2.47	9.81	4.46	12.15	12.66	11.67	19.25	23.10	5.02
F	43.20	51.88	39.36	26.90	43.84	40.57	34.30	43.98	43.36	40.54	35.43
<b>A'KF</b>											
A'	51.34	32.14	49.54	62.73	45.43	52.97	62.59	43.25	37.81	39.47	55.84
K	4.36	5.67	17.44	14.76	9.32	3.64	3.96	16.39	10.43	5.22	12.81
F	44.30	62.19	33.02	22.51	45.25	43.39	33.45	40.37	51.77	55.31	31.36
Sample	K7_198	K7_202,86	K7_203	K15_52	K15_85	K15_131	K15_217	K15_257	K15_359		
Element/%	Andesite	Andesite	Andesite	Andesite	Andesite	Andesite	Andesite	Andesite	Andesite	Andesite	Andesite
<b>AFM</b>											
A	61.88	53.18	49.53	40.77	40.11	40.42	47.33	38.26	46.15		
F	41.39	30.15	34.49	25.13	25.14	24.97	41.23	24.94	22.44		
M	10.48	15.17	15.98	30.04	30.31	29.64	6.10	28.69	24.94		
<b>A'CF</b>											
A'	56.60	40.39	38.28	34.25	28.74	29.19	54.28	37.43	46.25		
C	13.26	28.04	27.42	26.15	27.45	25.57	3.17	19.02	11.43		
F	30.15	31.57	34.29	39.60	43.81	45.23	42.55	43.55	42.33		
<b>A'KF</b>											
A'	57.61	40.74	36.66	30.11	20.69	23.92	46.84	34.64	53.57		
K	15.77	13.70	10.87	13.65	15.31	10.79	15.92	13.42	2.81		
F	26.62	45.56	52.47	56.24	64.00	65.29	37.23	51.95	43.62		

in which five samples describe biotite alteration and one, both chlorite. As a result of this variability, it can be stated that the current composition of Mangodara volcanic rocks is strongly influenced by alteration with gain of K<sub>2</sub>O, CaO, FeO and MgO. This has led to the stability of different minerals under the prevailing conditions of the amphibolite facies. Ti, Al, Zr, Y, Nb, Th, Cr, Co, and REE are considered to be immobile during hydrothermal alteration [52] [53] [54]. We evaluated volcanic rocks after hydrothermal alteration by plotting Zr vs Hf and

Y vs Ho. For the overall rocks, the results show a positive correlation regarding Zr vs Hf ( $R^2 = 0.82$ ) and Y vs Ho ( $R^2 = 0.80$ ) (**Figure 7(a)** and **Figure 7(b)**) with  $R^2$  as the correlation coefficient. This shows that Zr, Hf, Y and Ho are immobile during secondary processes and their concentration can be used to infer litho-geochemical classification.

#### 4.2.3. Geochemical Mobility in Relationship with Mineralization

##### 1) Major and traces elements distribution

The major elements of mineralized metarhyolite and metaandesites were normalized with the major elements of unmineralized metarhyolite and metaandesites, respectively, to determine their enrichment or depletion in the mineralized zone relative to the unmineralized zone (**Figure 8(a)** and **Figure 8(b)**). The major elements of mineralized metarhyolites and metaandesites respectively show enrichment in  $\text{Fe}_2\text{O}_3$  and  $\text{K}_2\text{O}$  and depletion respectively in  $\text{MgO}$ ,  $\text{Al}_2\text{O}_3$ ,  $\text{CaO}$ ,  $\text{SiO}_2$ ,  $\text{Na}_2\text{O}$ ,  $\text{P}_2\text{O}_5$  and  $\text{MgO}$ ,  $\text{Al}_2\text{O}_3$ ,  $\text{CaO}$ ,  $\text{SiO}_2$ .  $\text{TiO}_2$  is immobile in the two lithologies. To determine trace elements enrichment or depletion, we have estimated local thresholds for unmineralized metarhyolites and metaandesites (**Table 3**)

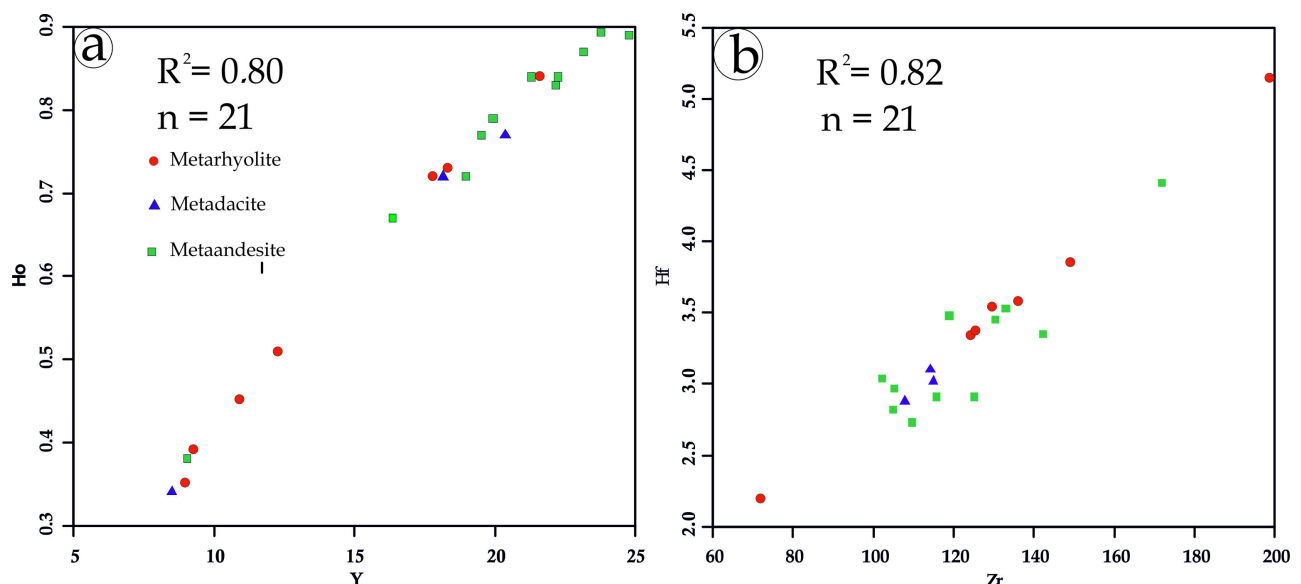


**Figure 7.** (a) binary Y/Ho diagram. (b) Zr/Hf binary diagram.

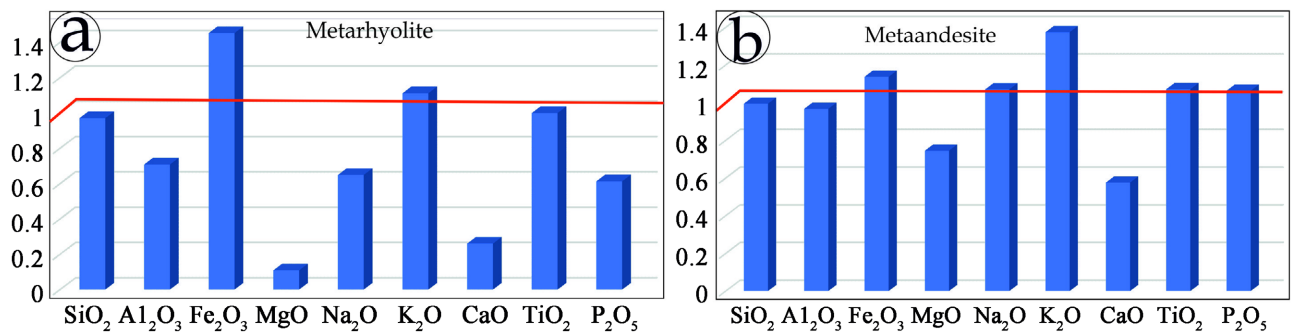


**Figure 8.** Comparison of major element value in samples from mineralized and unmineralized zones.

**Table 3.** Statistical summary of trace element data (in ppm) of rock samples from the Mangodara sector. Q1 = 1<sup>st</sup> quartile; Q2 = Medium; Q3 = third quartile; MAD = Median of Absolute Deviation from data median; EF = Enrichment factor.

	Au	Ag	As	Ba	Bi	Co	Cr	Cu	Eu	La	Mo	Ni	Pb	S	Sb	Sc	Sn	V	Zn
<b>Mineralized metarhyolite (n = 3)</b>																			
Minimum	0.03	0.25	19.70	411.10	0.15	20.90	78.00	53.00	1.00	23.90	1.70	36.00	5.90	3.11	3.54	16.40	0.80	101.00	14.00
5 <sup>th</sup> %le	0.04	0.25	31.64	467.63	0.15	21.41	81.60	54.70	1.00	24.07	1.74	37.50	8.01	3.15	3.64	16.77	0.81	101.50	14.40
25 <sup>th</sup> %le (Q1)	0.06	0.25	79.40	693.75	0.16	23.45	96.00	61.50	1.02	24.76	1.90	43.50	16.45	3.33	4.05	18.25	0.85	103.50	16.00
50 <sup>th</sup> %le (Median)	0.08	0.25	139.10	976.40	0.33	26.00	114.00	70.00	1.03	25.62	2.10	51.00	27.00	3.55	4.56	20.10	0.90	106.00	18.00
75 <sup>th</sup> %le (Q3)	3.77	0.68	144.55	1441.70	0.35	29.80	123.50	79.00	1.30	33.38	2.80	64.50	29.20	4.40	6.05	20.95	1.00	126.00	55.50
<b>Mineralized metarhyolite (n = 3)</b>																			
95 <sup>th</sup> %le	6.71	1.02	148.91	1813.94	0.36	32.84	131.10	86.20	1.52	39.59	3.36	75.30	30.96	5.07	7.23	21.63	1.08	142.00	85.50
Maximum	7.45	1.10	150.00	1907.00	0.26	33.60	133.00	88.00	1.57	41.14	3.50	78.00	31.40	5.24	7.53	21.80	1.10	146.00	93.00
MAD	2.47	0.28	43.43	498.63	0.04	4.23	18.33	11.66	0.19	5.74	0.60	14.00	8.50	0.71	1.33	1.80	0.10	15.00	26.33
Mean	2.52	0.53	102.93	1098.17	0.19	26.83	108.33	70.33	1.20	30.22	2.43	55.00	21.43	3.97	5.21	19.43	0.93	117.67	41.67
Std. deviation	4.27	0.49	72.29	755.35	0.06	6.39	27.93	17.50	0.32	9.50	0.95	21.28	13.63	1.12	2.07	2.76	0.15	24.66	44.50
Skewness	0.71	0.71	-0.69	0.29	0.62	0.24	-0.36	0.03	0.70	0.68	0.57	0.33	-0.63	0.58	0.52	-0.42	0.38	0.67	0.70
<b>Unmineralized metarhyolite (n = 4)</b>																			
Minimum	0.05	0.25	10.50	301.80	0.04	14.00	83.00	31.00	0.76	19.73	0.80	31.00	4.50	1.33	4.58	18.90	0.60	113.00	29.00
5 <sup>th</sup> %le	0.05	0.25	19.94	338.19	0.04	15.29	83.30	32.95	0.79	19.98	0.88	31.90	4.94	1.50	4.84	19.07	0.71	113.45	33.35
25 <sup>th</sup> %le (Q1)	0.06	0.25	57.68	483.75	0.04	20.45	84.50	40.75	0.92	20.98	1.18	35.50	6.68	2.18	5.89	19.73	1.13	115.25	50.75
50 <sup>th</sup> %le (Median)	0.06	0.25	89.65	574.75	0.08	23.10	92.50	50.50	1.06	22.60	1.45	38.50	13.80	2.55	7.61	20.05	1.35	116.50	85.00
75 <sup>th</sup> %le (Q3)	0.08	0.25	1092.85	679.15	0.13	26.25	110.75	66.50	1.16	25.03	2.18	52.25	20.73	2.67	11.22	20.23	1.43	122.25	115.75
95 <sup>th</sup> %le	0.12	0.25	3461.53	856.87	0.19	32.61	136.55	89.30	1.19	27.98	3.56	81.65	21.99	2.74	16.80	20.53	1.49	134.85	124.75
Maximum	0.13	0.25	4053.70	901.30	0.20	34.20	143.00	95.00	1.20	28.72	3.90	89.00	22.30	2.76	18.19	20.60	1.50	138.00	127.00
MAD	0.02	-	1018.92	165.05	0.05	5.30	18.75	19.25	0.15	2.85	0.85	15.25	7.65	0.40	4.04	0.45	0.25	6.50	38.00
Mean	0.07	0.25	1060.87	588.15	0.10	23.60	102.75	56.75	1.02	23.41	1.90	49.25	13.60	2.30	9.50	19.90	1.20	121.00	81.50
Std. deviation	0.04	-	1995.61	246.48	0.08	8.28	27.89	27.62	0.20	3.91	1.37	26.76	8.95	0.66	6.06	0.72	0.41	11.46	45.86
Skewness	1.03	NaN	1.15	0.18	0.62	0.21	0.92	0.67	-0.46	0.59	0.95	1.09	-0.02	-1.03	0.87	-0.68	-1.02	1.08	-0.14

Continued

mineralized metaandesite (n = 4)												
Minimum	–	0.25	12.20	561.70	0.09	19.60	77.00	35.00	1.00	22.02	1.60	25.00
5 <sup>th</sup> %le	0.01	0.25	17.26	585.63	0.09	19.92	77.75	35.45	1.00	22.23	1.66	25.90
25 <sup>th</sup> %le (Q1)	0.03	0.25	37.48	681.33	0.11	21.18	80.75	37.25	1.02	23.09	1.90	29.50
50 <sup>th</sup> %le (Median)	0.33	0.25	61.00	789.05	0.19	22.00	91.50	43.00	1.06	24.46	2.05	31.00
75 <sup>th</sup> %le (Q3)	0.95	0.59	1053.88	869.23	0.31	24.85	110.25	50.50	1.11	26.18	3.25	33.50
95 <sup>th</sup> %le	1.73	1.40	3400.54	898.81	0.43	30.97	132.45	56.50	1.17	27.85	6.01	39.50
Maximum	1.92	1.60	3987.20	906.20	0.46	32.50	138.00	58.00	1.19	28.27	6.70	41.00
MAD	0.62	0.33	1001.30	120.05	0.13	3.38	20.00	8.25	0.06	2.07	1.30	4.00
Mean	0.65	0.59	1030.35	761.50	0.23	24.03	99.50	44.75	1.08	24.80	3.10	32.00
Std. deviation	0.90	0.68	1971.41	154.47	0.17	5.77	27.67	10.44	0.08	2.71	2.41	6.63
Skewness	0.85	1.15	1.15	-0.43	0.59	1.01	0.73	0.38	0.67	0.35	1.13	0.51
EF	20.13	3.14	34.24	1.01	3.27	0.98	0.96	0.81	0.95	1.06	2.13	0.87
Unmineralized metaandesite (n = 7)												
Minimum	–	0.11	6.70	266.40	0.02	15.70	56.00	12.00	0.96	20.38	0.80	23.00
5 <sup>th</sup> %le	0.01	0.15	7.57	299.85	0.02	16.57	61.10	13.50	0.96	20.97	0.92	23.90
25 <sup>th</sup> %le (Q1)	0.03	0.25	9.95	520.80	0.03	19.85	82.00	18.50	0.99	22.67	1.30	26.50
50 <sup>th</sup> %le (Median)	0.04	0.25	11.70	697.50	0.08	23.70	99.00	45.00	1.05	23.43	1.50	29.00
75 <sup>th</sup> %le (Q3)	0.06	0.25	19.25	756.65	0.09	24.10	110.50	47.00	1.17	25.46	1.75	35.00
95 <sup>th</sup> %le	0.08	0.25	118.32	880.26	0.10	26.29	127.30	53.30	1.26	27.05	2.15	54.50
Maximum	0.08	0.25	158.10	927.30	0.11	27.10	130.00	56.00	1.27	27.12	2.30	62.00
MAD	0.02	0.02	24.28	161.80	0.03	2.84	18.71	14.42	0.09	1.76	0.34	8.00
Mean	0.04	0.23	33.56	635.16	0.06	22.06	95.71	34.86	1.08	23.88	1.53	33.86
Std. deviation	0.03	0.05	55.25	231.70	0.04	3.87	25.69	17.83	0.12	2.42	0.48	13.25
Skewness	0.19	-2.04	1.99	-0.55	-0.06	-0.46	-0.19	-0.22	0.47	0.16	0.10	1.56
EF	1.00	1.00	1.00	1.00	1.00	1.00	1.00	1.00	1.00	1.00	1.00	1.00

equal to the median of the data plus twice the median absolute deviation (MAD) for each geochemical element [55]. Then, we defined the enrichment factor (EF) according to the following formula:

$$EF = [\text{Median} + 2\text{MAD}]_{\text{mineralized rock sample group}} / [\text{Median} + 2\text{MAD}]_{\text{Unmineralized rock sample group}}$$

Comparison of trace elements data from mineralized and unmineralized metarhyolite show enrichment in Au, Ag, Ba, Bi, Cr, Cu, Eu, La, Mo, Ni, Pb, S, Sc, V and depletion in As, Sb, Co, Sn, Zn in mineralized metahryolite. Regarding metaandesites we note enrichment in Au, Ag, As, Mo, S, Sb and depletion in Co, Sn, Zn, Bi, Cr, Cu, Eu, Ni, Pb, Sc in mineralized metaandesites. Ba, La, V are immobile in metaandesites (**Table 3**).

## 2) Principal Component analysis of major elements

To better characterize the geochemical processes associated with each type of alteration, we undertook geochemical balance based on Principal Component analysis (PCA) on major elements. The variables are  $\text{SiO}_2$ ,  $\text{Al}_2\text{O}_3$ ,  $\text{Fe}_2\text{O}_3$ ,  $\text{MgO}$ ,  $\text{CaO}$ ,  $\text{Na}_2\text{O}$ ,  $\text{K}_2\text{O}$ ,  $\text{P}_2\text{O}_5$ ,  $\text{TiO}_2$ ,  $\text{MnO}$ . The mineralized metarhyolite samples are described by two main components, PC1 and PC2 explained 56.72% and 43.32% of multivariate data variability, respectively. PC1 represents opposing associations of  $\text{SiO}_2\text{-CaO}\text{-TiO}_2\text{-MgO}\text{-MnO}\text{-P}_2\text{O}_5$  and  $\text{Na}_2\text{O}\text{-K}_2\text{O}\text{-Al}_2\text{O}_3\text{-Fe}_2\text{O}_3$  reflecting quartz, carbonate and biotite in the proximal zone and white mica in the mineralized zone. PC2 represents opposing associations of  $\text{SiO}_2\text{-Na}_2\text{O}\text{-K}_2\text{O}\text{-Al}_2\text{O}_3\text{-TiO}_2\text{-MgO}\text{-MnO}\text{-P}_2\text{O}_5$  and  $\text{CaO}\text{-Fe}_2\text{O}_3$  reflecting protolith and metamorphism minerals close to the mineralization and carbonate veins associated with the sulphide mineralization. The PC1-PC2 biplot (**Figure 9(a)**) describes major elements associations representing the main process associated with mineralization, in which  $\text{Na}_2\text{O}\text{-K}_2\text{O}\text{-Al}_2\text{O}_3$  describes potassic and alumina alteration;  $\text{SiO}_2\text{-TiO}_2\text{-MgO}$  describes biotite alteration;  $\text{Fe}_2\text{O}_3$  describes metal;  $\text{CaO}$  describes carbonate alteration. In unmineralized metarhyolite, PC1 and PC2 explain 76.98% and 18.58% of multivariate data variability, respectively. PC1 represents opposing associations of  $\text{SiO}_2\text{-Na}_2\text{O}\text{-K}_2\text{O}$  and  $\text{CaO}\text{-MgO}\text{-MnO}\text{-P}_2\text{O}_5\text{-Al}_2\text{O}_3\text{-Fe}_2\text{O}_3$  reflecting the protolith. PC2 represents opposing associations of  $\text{Al}_2\text{O}_3\text{-TiO}_2$  and  $\text{MgO}\text{-Fe}_2\text{O}_3$  that reflect metamorphism. In the PC1-PC2 biplot (**Figure 9(b)**) that describes major associations representing major processes associated with unmineralized metarhyolites,  $\text{SiO}_2\text{-Na}_2\text{O}\text{-K}_2\text{O}$  describes feldspar and sericite;  $\text{CaO}\text{-MgO}\text{-MnO}\text{-P}_2\text{O}_5\text{-Fe}_2\text{O}_3$  describes ferromagnesian minerals;  $\text{Al}_2\text{O}_3$  describes alumina alteration. In Metadacite PC1 and PC2 explain 72.19% and 27.80% of multivariate data variability, respectively. PC1 represents opposing associations of  $\text{Na}_2\text{O}\text{-SiO}_2\text{-Al}_2\text{O}_3\text{-TiO}_2$  and  $\text{CaO}\text{-MgO}\text{-MnO}\text{-P}_2\text{O}_5\text{-Fe}_2\text{O}_3\text{-K}_2\text{O}$  that reflect the metadacites protolith. In the PC1-PC2 biplot (**Figure 9(c)**),  $\text{Na}_2\text{O}\text{-SiO}_2\text{-Al}_2\text{O}_3$  describes the plagioclase;  $\text{CaO}\text{-MgO}\text{-MnO}\text{-P}_2\text{O}_5\text{-Fe}_2\text{O}_3$  describes ferromagnesian and hydrothermal alteration;  $\text{P}_2\text{O}_5\text{-K}_2\text{O}$  describes potassic alteration. Regarding metaandesites, PC1 and PC2 explain 56.15 and 26.72 of multivariate data variability, respectively). PC1 represents opposing associations of  $\text{SiO}_2\text{-K}_2\text{O}$  and  $\text{Na}_2\text{O}\text{-CaO}\text{-MgO}\text{-MnO}\text{-P}_2\text{O}_5\text{-Al}_2\text{O}_3\text{-Fe}_2\text{O}_3$

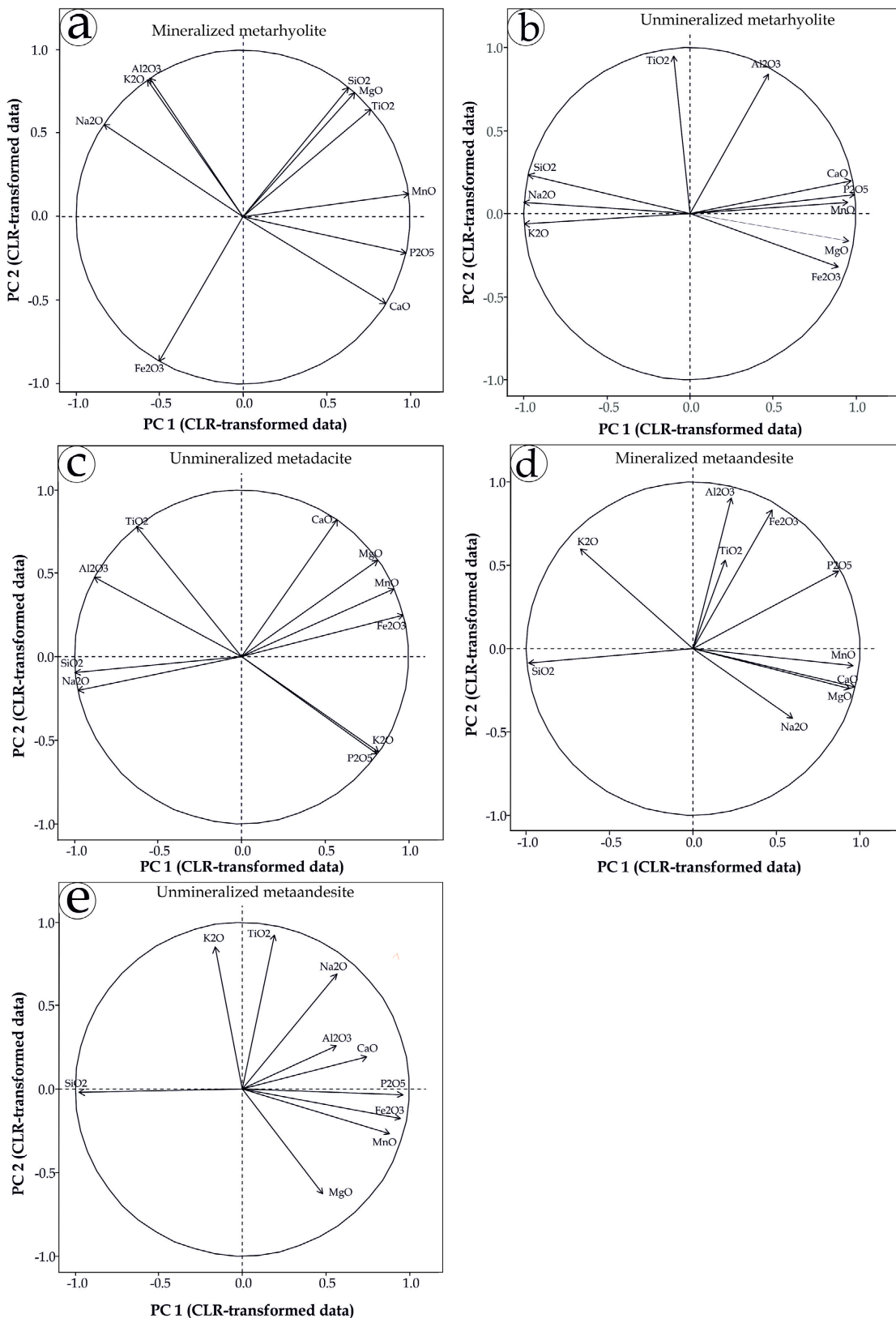


**Figure 9.** Biplot of varimax rotated principal component of major element data for three lithologies (mineralized metarhyolites and metaandesites, unmineralized metarhyolites and metadesites; metadacites) of the Mangodara sector.

that reflect potassic alteration and protolith, respectively. PC2 represents opposing associations of  $K_2O$ - $P_2O_5$ - $Al_2O_3$ - $Fe_2O_3$ - $TiO_2$  and  $Na_2O$ - $CaO$ - $MgO$ -( $SiO_2$ - $MnO$ ) which respectively reflect potassic and aluminous alteration associated with mineralization and carbonate and biotite alteration in the proximal zone. In the PC1-PC2 biplot (**Figure 9(d)**),  $Na_2O$ - $CaO$ - $MgO$  describes metamorphism;  $Al_2O_3$ - $Fe_2O_3$  describes aluminous alteration associated with sulphide mineralization;  $SiO_2$ - $K_2O$  describes sericite and siliceous alteration. In unmineralized metaandesite PC 1 and PC 2 explain 50.36% and 26.52% of multivariate data variability, respectively). PC1 represents opposing associations of  $SiO_2$  (- $K_2O$ ) and  $Na_2O$ - $CaO$ - $MgO$ - $MnO$ - $P_2O_5$ - $Al_2O_3$ - $Fe_2O_3$  that reflect respectively the silica alteration and the protolith. In the PC1-PC2 biplot (**Figure 9(e)**),  $Na_2O$ - $CaO$ - $Al_2O_3$  describes plagioclase;  $MgO$ - $MnO$ - $Al_2O_3$ - $Fe_2O_3$  describes the ferromagnesian minerals of the protolith;  $K_2O$ - $TiO_2$  describes the accessory minerals of the protolith.

### 3) Principal component analysis of trace elements

In the mineralized metarhyolites, PC1 and PC2 explain 58.31% and 41.68% of multivariate data variability, respectively). PC1 represents opposing associations of Au-As-Ba-Cu-Eu-La-Mo-Ni-S-Sc-Zn (-Cr-Pb) and V-Sb-Co-Sn-Ag-Bi which reflect respectively: 1) hydrothermal alteration and base metal associated with gold mineralization and 2) base metal sulphide mineralization. PC2 represents opposing associations of V-Sn-Ag-Cr-Pb-Sc-Co-Ba-Ni and Bi-Sb-As-Cu which reflect respectively: 1) hydrothermal alteration and 2) sulphide mineralization. The PC1-PC2 biplot (**Figure 10(a)**) describes the associations of trace elements representing the main processes associated with the mineralization of the Mangodara sector: 1) Au-Ba-Cu-Eu-La-Mo-Ni-S-Zn describes alteration halos and base metal associated with gold mineralization; 2) V-Sn-Co-Ag describes base metal enrichment close to gold mineralization. In unmineralized metarhyolite, PC1 and PC2 explain 54.37% and 31.27% of multivariate data variability, respectively. PC1 represents opposing associations of Au-Mo-Bi-As-Cr-Ni-Sb-Co-S-Sn-Pb (-Cu-Sc) and La-Eu (-V-Zn-Ba) which reflect respectively: 1) base metal associated with gold mineralization and 2) protolith. PC2 represents opposing associations of Sn-Pb-Ba-La-Eu and V-Zn-Cu-S (-Sc-Co-Sb) that reflect hydrothermal alteration and base metal enrichment, respectively. The PC1-PC2 biplot (**Figure 10(b)**) describes associations of trace elements representing the main processes associated with unmineralized metarhyolites from the Mangodara area: 1) Au-Mo-Bi-As-Cr-Ni-Sb-Co describe unmineralized Au-bearing metarhyolites; 2) S-Cu-Zn-V-Sc describes base metal enrichment. In mineralized metaandesites, PC 1 and PC 2 explain 50.32% and 38.81% of multivariate data variability, respectively. PC1 represents opposing associations of Au-S-Sb-As-Ag-Bi (-Ba-Sn-La-Cr) and V-Sc-Zn-Eu-Cu (-Co-Mo-Pb) which respectively reflect: 1) hydrothermal alteration and base metal associated with gold mineralization and 2) base metal enrichment. In the PC1-PC2 biplot (**Figure 10(c)**), Au-S-Sb-As-Ag-Bi describe sulphide mineralization associated with gold; Ba-Sn-La-Cr-Co-Mo-Pb

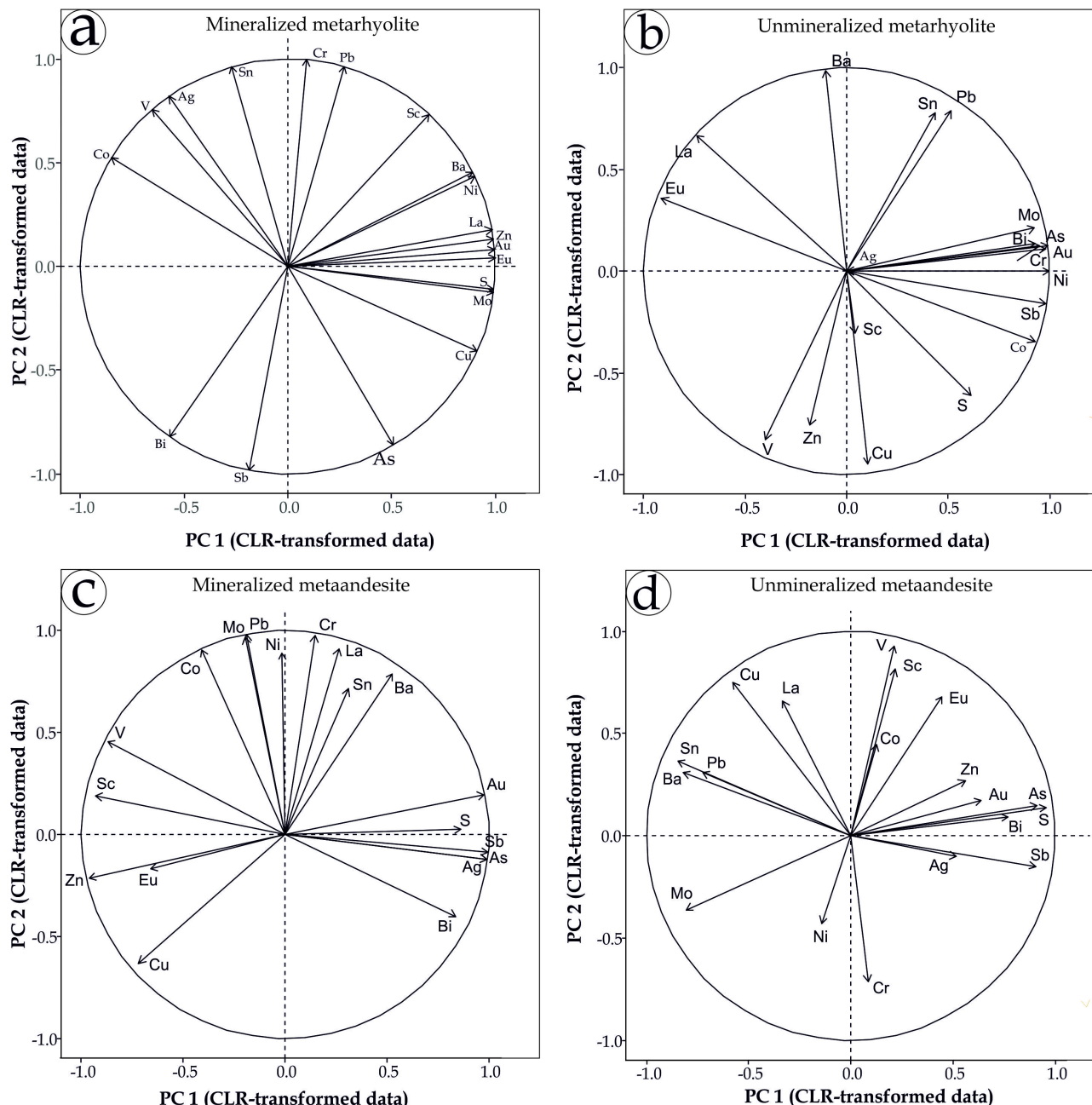


**Figure 10.** Biplot of varimax rotatidate principal component trace element data for two lithologies (mineralized metarhyolites and metaandesites, unmineralized metarhyolites and metandesites) of the Mangodara sector.

describe hydrothermal alteration halos and V-Sc-Zn-Eu-Cu describe base metal enrichment. In unmineralized metaandesite, PC1 and PC2 explain 39.43% and 23.78% of multivariate data variability, respectively where PC1 represents opposing associations of Au-As-S-Bi-Sb-Zn-Eu-Ag(-Sc-V-Co-Cr) and Mo-Ba-Sn-Pb-Cu (-La-Ni). These associations respectively reflect: 1) base metal enrichment associated with gold mineralization and 2) hydrothermal alteration and base metal enrichment. PC2 represents opposing associations of Cu-La-V-Sc-Eu (-Sn-Pb-Ba-Co-Zn-Au-S-Bi-As) and Ni-Cr-Mo (-Sb373-Ag) which respectively reflect: 1)

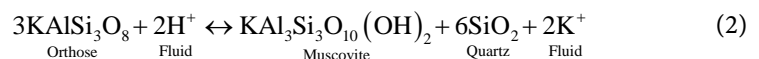
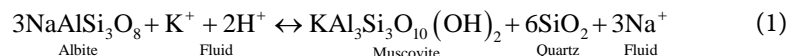
hydrothermal alteration and sulfides and 2) Primary mineralization. In the PC1-PC2 biplot (**Figure 10(d)**); Au-As-S-Bi-Sb-Zn-Ag describe sulphide mineralization associated with gold mineralization; Sc-V-Co-Eu describe hydrothermal alteration associated with gold mineralization; and Ba-Sn-Pb-Cu-La describe hydrothermal alteration; 3) Mo-Ni describe the primary mineralization

## 5. Discussions

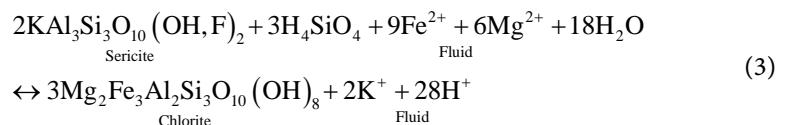
### 5.1. Alteration and Mineral Paragenesis

Potential in mineral resources in the Banfora Birimian (Paleoproterozoic) greenstone belts is still debated since no world-class deposits are yet discovered in the belt despite an intensive exploration campaign [43]. In this paper, we are dealing with the possible volcanic-hosted gold mineralization and base metal enrichment. In hydrothermal deposits, secondary mineral assemblages correlated with geochemical compositions can be used as a vector for tracking gold mineralization [50] [56] [57] [58]. Mineral paragenetic associations are 1) primary mineral assemblage; 2) Metamorphic index minerals (kyanite, staurolite, garnet) typical of amphibolite facies, but suggesting predominant aluminous alteration, are overprinted by sericite-chlorite-biotite-carbonate alteration. In the Eastmain River deposit, [59] distinguished two different alteration assemblages which are both associated with the ore: a prograde garnet assemblage, and an epidote assemblage which locally retrogrades the garnet assemblage. Such alteration is documented at Bousquet 2 - Dumagami in Canada [60] where andalusite - kyanite - pyrophyllite assemblages are interpreted to represent the metamorphic equivalent of synvolcanic alteration produced by oxidative hydrothermal and acid fluids, relevant to advanced clay-like alteration. In opposite of andalusite and kyanite from Bousquet 2-Dumagami resulting in low-temperature metamorphism, those of Mangodara sector implying kyanite, staurolite, garnet and sillimanite originate from high temperature. In metamorphosed and deformed terranes like at Caho Ortegal, northwestern Spain of Sapey, kyanite, staurolite bearing gneisses are related to high-temperature metamorphism [61] [62]. Aluminous alteration (kyanite-staurolite-garnet) and plagioclase-quartz-white mica-staurolite-kyanite-garnet—sulphide at Mangodara are mainly hosted by metarhyolites. At Korpela, K-Al-Mg-Fe-S type alteration (muscovite, aluminosilicates, staurolite and garnet) is hosted by andesite and rhyolite [57]. In the current study, we assume kyanite and staurolite alteration corresponds to the first stage of metamorphism. The epitaxial intergrowth between kyanite and staurolite suggests concomitant development and that this assemblage was stable before major metamorphism [63]. In our case, assemblage is overprinted by sericite, and chloritoid, chlorite, suggests retrograde metamorphism. Sericitization causes losses of Ca and Na and is generally accompanied by gain (Equation (1)) or loss (Equation (2)) of K depending on the altered minerals [64]. Sericite alteration is ubiquitous in all selected samples from the study area. Indeed, the loss of Na in the rock and the contribution of K in solution allows the replacement of albite

by white mica and the crystallization of quartz [57] as shown in the following reaction (Equation (1)):



Mineralized samples show strong Na depletion compared to unmineralized samples. Sillimanite occurs in micaceous beds in metarhyolites. The muscovite surrounding the corroded kyanite suggests a change in (P-T) conditions such that the kyanite is no longer in equilibrium [65]. These reactions lead to an increase of aluminum content in the altered rock, producing during metamorphism, the recrystallization of sillimanite porphyroblasts [57]. Chloritization is generally associated to sericitization and this is characterized by the progressive transformation of sericite into chlorite (Equation (3)) in the core of the Volcanogenic Massive Sulfide (VMS) hydrothermal system, resulting in Fe and/or Mg gains [2].



This chemical reaction (Equation (3)) leads to an increase of aluminum and iron concentrations in the altered rock producing during retrograde metamorphism, and recrystallization of chloritoid porphyroblasts.

## 5.2. Relationships between Hydrothermal Alteration and Mineralization

In the subsequent works Zr, Y, Ti and Al are immobile in volcanic rocks affected by hydrothermal fluid [53] [54] [64] [66]. The depletion of  $\text{Al}_2\text{O}_3$  in the mineralized zone containing kyanite and staurolite porphyroblasts is a result of the corroded species. In opposite  $\text{Al}_2\text{O}_3$  is stable in the mineralized metaandesites. The PC1-PC2 biplot (**Figure 9(a)**) that describes the opposition such  $\text{Na}_2\text{O}$ - $\text{K}_2\text{O}$ - $\text{Al}_2\text{O}_3$  and  $\text{Fe}_2\text{O}_3$  suggests that the majority sulphide (pyrite and pyrrhotite) is not linkable to the various hydrothermal alterations in mineralized metarhyolites. Aluminou alteration is associated with mineralized metaandesites (**Figure 9(d)**). Mineralized metarhyolites are enriched in Au, Ag, Ba, Bi, Cr, Cu, Eu, La, Mo, Ni, Pb, S, Sc, V and depleted in As, Sb, Co, Sn, Zn while mineralized metaandesites are enriched in Au, Ag, As, Mo, S, Sb and depleted in Co, Sn, Zn, Bi, Cr, Cu, Eu, Ni, Pb, Sc. Ba, La, V are immobile in metaandesites. Depletion in As, Sb in the mineralized metarhyolites and Au + As + Sb association in the unmineralized samples are not part of Au system in the Manga-dara sector. Au mineralization is generally accompanied by enrichment in  $\text{SiO}_2$ ,  $\text{K}_2\text{O}$ , Rb, Hg, Sb, Se, Te, Tl and Cs and depletion of  $\text{Na}_2\text{O}$ - $\text{CaO}$ - $\text{MgO}$  and Ba [1] [67] [68] [69].

### 5.3. Mobility and Guide for Exploration

Argillic alteration provides a useful mineralogical guide for Au mineralization of Mangodara sector [23]. We argue that the quartz-sericite-staurolite-kyanite-sulphide assemblage in the metarhyolite is typical of the proximal footprint hosting Au mineralization. Sulphides are the most important mineral assemblages responsible for Au mineralization in the Mangodara sector, as indicated by the mobility of elements causing enrichment in K<sub>2</sub>O, FeO and depletion in other major elements: CaO, MgO, Na<sub>2</sub>O, Al<sub>2</sub>O<sub>3</sub>, SiO<sub>2</sub>. The enrichment factor of Au, Ag, S in the mineralized samples and their association Ag + S shows they can be used as an exploration guide in the Mangodara sector. Indeed, Au mineralization of that sector is of the argentiferous type [23]. Therefore, the well-known indicators like Ag, As, Sn should be moderately considered here at Mangodara

## 6. Conclusions

Gold and base metal occurrences of Mangodara sector are hosted in the highly metamorphosed altered volcanic rock made up of metarhyolites, metadacites and metaandesites. The metamorphism reached the amphibolite facies according to index minerals like kyanite, staurolite, garnet and sillimanite. The study of the mobility of geochemical elements carried out along two boreholes revealed the following points: 1) sulphides are the most important mineral assemblages responsible for Au mineralization in the Mangodara sector; 2) The geochemistry of the mineralized zone is characterized by the association of Au + Ba + Cu + Eu + La + Mo + Ni + S in metarhyolites and of Au + S + Sb + As + Ag + Bi in metaandesites; 3) The concentration of Fe<sub>2</sub>O<sub>3</sub>, S and Cu is attributed to the presence of Fe-Cu sulphides (pyrite, pyrrhotite and chalcopyrite) indicating that sulphides are vectors of the mineralization zone in the Mangodara sector; 4) Addition of CaO, MgO; Na<sub>2</sub>O, Al<sub>2</sub>O<sub>3</sub>, K<sub>2</sub>O, SiO<sub>2</sub> is a function of the resulting alteration, as evidenced by aluminous alteration, sericitization, chloritization, biotitization, and carbonatation; 5) Metal associations Ag + S can be used as a guide for Au exploration in the Mangodara sector; 6) The well-known indicators like Ag, As, Sn seems therefore not to be mandatory as indicators of Au for exploration purposes in the Mangodara sector

## Acknowledgments

This work is part of the first author—Bernadin Gnamou (BG) PhD work. The author is grateful to the ministère de l'enseignement supérieur et de la recherche scientifique et de l'innovation for granting three years scholarship through the Programme d'Appui à l'Enseignement Supérieur (PAES).

## Conflicts of Interest

The authors declare no conflicts of interest regarding the publication of this paper.

## References

- [1] Wang, C., Carranza, E.J.M., Zhang, S., Zhang, J., Liu, X., Zhang, D., Sun, X. and Duan, C. (2013) Characterization of Primary Geochemical Haloes for Gold Exploration at the Huanxiangwa Gold Deposit, China. *Journal of Geochemical Exploration*, **124**, 40-58. <https://doi.org/10.1016/j.gexplo.2012.07.011>
- [2] Genna, D., Gaboury, D. and Roy, G. (2014) Evolution of a Volcanogenic Hydrothermal System Recorded by the Behavior of LREE and Eu: Case Study of the Key Tuffite at Bracemac-McLeod Deposits, Matagami, Canada. *Ore Geology Reviews*, **63**, 160-177. <https://doi.org/10.1016/j.oregeorev.2014.04.019>
- [3] Manya, S. (2016) Petrogenesis and Emplacement of the TTG and K-Rich Granites at the Buzwagi Gold Mine, Northern Tanzania: Implications for the Timing of Gold Mineralization. *Lithos*, **256-257**, 26-40. <https://doi.org/10.1016/j.lithos.2016.03.025>
- [4] Manya, S. (2017) Characterization of Geochemical Alteration Halo Associated with Gold Mineralization at the Buzwagi Mine, Northern Tanzania. *Journal of African Earth Sciences*, **129**, 136-145. <https://doi.org/10.1016/j.jafrearsci.2017.01.006>
- [5] Sillitoe, R.H., Magaranov, G., Mladenov, V., Robert, A. and Creaser, R.A. (2020) Rosen, Bulgaria: A Newly Recognized Iron Oxide-Copper-Gold District. *Economic Geology*, **115**, 481-488. <https://doi.org/10.5382/econgeo.4731>
- [6] Vasilopoulos, M., Molnár, F., O'Brien, H., Lahaye, Y., Lefèvre, M., Richard, A., André-Mayer, A.S., Ranta, J.P. and Talikka, M. (2021) Geochemical Signatures of Mineralizing Events in the Juomasuo Au-Co Deposit, Kuusamo Belt, Northeastern Finland. *Mineralium Deposita*, **56**, 1195-1222. <https://doi.org/10.1007/s00126-020-01039-8>
- [7] Migdisov, A.A., Williams-Jones, A.E. and Wagner, T. (2009) An Experimental Study of the Solubility and Speciation of the Rare Earth Elements (III) in Fluoride- and Chloride-Bearing Aqueous Solutions at Temperatures up to 300°C. *Geochimica et Cosmochimica Acta*, **73**, 7087-7109. <https://doi.org/10.1016/j.gca.2009.08.023>
- [8] Pokrovski, G.S., Maria, A., Kokh, M.A., Damien Guillaume, D., Dubessy, J., *et al.* (2015) Sulfur Radical Species from Gold Deposits on Earth. *Proceedings of the National Academy of Sciences of the United States of America*, **112**, 13484-13489. <https://doi.org/10.1073/pnas.1506378112>
- [9] Rollinson, H.R. and Pease, V. (2021) Using Geochemical Data: To Understand Geological Processes. 2nd Edition, Cambridge University Press, Cambridge. <https://doi.org/10.1017/9781108777834>
- [10] Guiraud, J. (2021) Les amas sulfurés volcanogènes à or, un nouveau potentiel de gisement dans le bouclier Guyanais: Exemple du gisement montagne d'or. Master's Thesis, Université du Québec à Montréal, Montréal.
- [11] Cann, J.R. (1970) Rb, Sr, Y, Zr et Nb dans certaines roches basaltiques du fond océanique. *Terre Planétaire Lettres scientifiques*, **10**, 7-11. [https://doi.org/10.1016/0012-821X\(70\)90058-0](https://doi.org/10.1016/0012-821X(70)90058-0)
- [12] Polat, A. and Hofmann, A.W. (2003) Altération et schémas géochimiques dans l'Isua 3, 7-3, 8 Ga ceinture de roches vertes, ouest du Groenland. *Precambrian Research*, **126**, 197-218. [https://doi.org/10.1016/S0301-9268\(03\)00095-0](https://doi.org/10.1016/S0301-9268(03)00095-0)
- [13] Taylor, S.R. and McLennan, S.M. (1985) The Continental Crust, Its Composition and Evolution. An Examination of the Geochemical Record Preserved in Sedimentary Rocks. Blackwell Scientific Publications, Oxford.
- [14] Napon, S. (1988) Le gisement d'amas sulfurés (Zn-Ag) de Perkoa dans la province du Sangyé (Burkina Faso—Afrique de l'Ouest): Cartographie, étude pétrographique, géochimique et métallogénique. Master's Thesis, University de Franche-Comté, Be-

sançon.

- [15] Kříbek, B., Zachariáš, J., Kněsl, I., Míková, J., Mihaljevič, M., Veselovský, F. and Bamba, O. (2016) Geochemistry, Mineralogy, and Isotope Composition of Pb, Zn, and Cu in Primary Ores, Gossan and Barren Ferruginous Crust from the Perkoa Base Metal Deposit, Burkina Faso. *Journal of Geochemical Exploration*, **168**, 49-64. <https://doi.org/10.1016/j.gexplo.2016.05.007>
- [16] Markwitz, V., Hein, K.A.A. and Miller, J. (2016) Compilation of West African Mineral Deposits: Spatial Distribution and Mineral Endowment. *Precambrian Research*, **274**, 61-81. <https://doi.org/10.1016/j.precamres.2015.05.028>
- [17] Ilboudo, H., Lombo, M., Wenmenga, U., Napon, S., Naba, S. and N'gom, P.M. (2017) Evidence of a Volcanogenic Massive Sulfide (Zn-PbCu-Ag) District within the Tiébélé Birimian (Paleoproterozoic) Greenstone Belts, Southern Burkina Faso (West-Africa). *Journal of African Earth*, **129**, 792-813. <https://doi.org/10.1016/j.jafrearsci.2017.01.020>
- [18] Augustin, J. and Gaboury, D. (2017) Paleoproterozoic Plume-Related Basaltic Rocks in the Mana Gold District in Western Burkina Faso, West Africa: Implications for Exploration and the Source of Gold in Orogenic Deposits. *Journal of African Earth Sciences*, **129**, 17-30. <https://doi.org/10.1016/j.jafrearsci.2016.12.007>
- [19] Goldfarb, R.J., André-Mayer, A.S., Jowitt, S.M. and Mudd, G.M. (2017) West Africa: The World's Premier Paleoproterozoic Gold Province. *Economic Geology*, **112**, 123-143. <https://doi.org/10.2113/econgeo.112.1.123>
- [20] Gauriau, J., Harlaux, M., André-Mayer, A.S., Eglinger, A., Richard, A., Fontaine, A., Lefebvre, M.G., Béziat, D., Villeneuve, J. and Lemarchand, D. (2020) Chemical and Boron Isotope Composition of Tourmaline from the Kiaka Orogenic Gold Deposit (Burkina Faso, West African Craton) as a Proxy for Ore-Forming Processes. *Mineralium Deposita*, **57**, 581-600. <https://doi.org/10.1007/s00126-020-01002-7>
- [21] Masurel, Q., Eglinger, A., Thébaud, N., Allibone, A., André-Mayer, A.S., McFarlane, H., Miller, J., Jessell, M., Aillères, L., Vanderhaeghe, O., Salvi, S., Baratoux, L., Perrouty, S., Begg, G., Fougerouse, D., Hayman, P., Wane, O., Tshibubudze, A., Parra-Avila, L., Kouamélan, A. and Amponsah, P.O. (2021) Paleoproterozoic Gold Events in the Southern West African Craton: Review and Synopsis. *Mineralium Deposita*, **57**, 513-537. <https://doi.org/10.1007/s00126-021-01052-5>
- [22] Thébaud, N., Eglinger, A., André-Mayer, A.S. and Kolb, J. (2022) Preface to the Thematic Issue on Mineral Systems of West Africa. *Mineralium Deposita*, **57**, 509-511. <https://doi.org/10.1007/s00126-022-01100-8>
- [23] Ilboudo, H., Wenmenga, U. and Sawadogo, S. (2017) Mise en évidence d'un assemblage à disthène—staurotide—grenat dans le secteur de Mangodara, ceinture de Banfora, Burkina Faso, Afrique de l'Ouest: Implication dans la genèse des gîtes minéraux polymétalliques. *Afrique Science*, **13**, 220-223.
- [24] Fontaine, A., Eglinger, A., Ada, K., André-Mayer A.S., Reisberg, L., Siebenaller, L., Le Mignot, E., Ganne, J. and Poujol, M. (2017) Geology of the World-Class Kiaka Polyphase Gold Deposit, West African Craton, Burkina Faso. *Journal of African Earth Sciences*, **126**, 96-122. <https://doi.org/10.1016/j.jafrearsci.2016.11.017>
- [25] Ouattara, A.S., Coulibaly, Y. and Kouadio, F.J.L.H. (2017) Les altérations hydrothermales associées à la minéralisation aurifère du gisement de Dougbafla (district d'Oumé-Hiré, centre-ouest de la Côte d'Ivoire). *European Scientific Journal*, **13**, 108-125. <https://doi.org/10.19044/esj.2017.v13n30p108>
- [26] Le Mignot, E., Siebenaller, L., Béziat, D., André-Mayer, A.S., Laurie Reisberg, L., Salvi, S., Velasquez, G., Zimmermann, C., Naré, A. and Franceschi, G. (2017) The

Paleoproterozoic Copper-Gold Deposits of the Gaoua District, Burkina Faso: Superposition of Orogenic Gold on a Porphyry Copper Occurrence? *Economic Geology*, **112**, 99-122. <https://doi.org/10.2113/econgeo.112.1.99>

- [27] Allou, G., Lionel, B.K.T.D., Inza, C. Eric, B.I. and Yacouba, C. (2022) Etude Metallogenique du Prospect Aurifère de Woulo-Woulo (Zone d'Afema, Sud-est de la Côte d'Ivoire). *European Scientific Journal*, **18**, 121. <https://doi.org/10.19044/esj.2022.v18n33p121>
- [28] Kouamelan, A.N. (1996) Géochronologie et Géochimie des Formations Archéennes et Protérozoïques de la Dorsale de Man en Côte d'Ivoire. Implications pour la Transition Archéen-protérozoïque. Master's Thesis, Université de Rennes I. France, Rennes.
- [29] Caby, R., Delor, C. and Agoh, O. (2000) Lithologie, Structure et métamorphisme des formations birimiennes dans la région d'Odienné (Côte d'Ivoire): Rôle majeur du diapirisme des plutons et des décrochements en bordure du craton de Man. *Journal of African Earth Sciences*, **30**, 351-374. [https://doi.org/10.1016/S0899-5362\(00\)00024-5](https://doi.org/10.1016/S0899-5362(00)00024-5)
- [30] Castaing, C., Billa, M., Milési, J.P., Thiéblemont, D., Le Métour, J., Egal, E., Donzeau, M., Guerrot, C., Cocherie, A., Chèvremont, P., Tegyey, M., Itard, Y., Zida, B., Ouedraogo, I., Kote, S., Kabore, B.E., Ouedraogo, C., Ki, J.C. and Zunino, C. (2003) Notice explicative de la carte géologique et minière du Burkina Faso à 1/1 000 000. Bureau de Recherches Géologiques et Minières (BRGM).
- [31] Rollinson, H. (2016) Archaean Crustal Evolution in West Africa: A New Synthesis of the Archaean Geology in Sierra Leone, Liberia, Guinea and Ivory Coast. *Precambrian Research*, **281**, 1-12. <https://doi.org/10.1016/j.precamres.2016.05.005>
- [32] Block, S., Baratoux, L., Zeh, A., Laurent, O., Bruguier, O., Jessell, M. and Bosch, D. (2016) Paleoproterozoic Juvenile Crust Formation and Stabilisation in the South-Eastern West African Craton (Ghana); New Insights from U-Pb-Hf Zircon Data and Geochemistry. *Precambrian Research*, **287**, 1-30. <https://doi.org/10.1016/j.precamres.2016.10.011>
- [33] Lompo, M. (2009) Geodynamic Evolution of the 2.25-2.0 Ga Palaeoproterozoic Magmatic Rocks in the Man-Leo Shield of the West African Craton. A Model of Subsidence of an Oceanic Plateau. *Geological Society of London*, **323**, 231-254. <https://doi.org/10.1144/SP323.11>
- [34] Lompo, M. (2010) Paleoproterozoic Structural Evolution of the Man-Leo Shield (West Africa). Key Structures for Vertical to Transcurrent Tectonics. *Journal of African Earth Sciences*, **58**, 19-36. <https://doi.org/10.1016/j.jafrearsci.2010.01.005>
- [35] Vidal, M., Gumiaux, C., Cagnard, F., Pouclet, A., Ouattara, G. and Pichon, M. (2009) Evolution of a Paleoproterozoic "Weak Type" Orogeny in the West African Craton (Ivory Coast). *Tectonophysics*, **477**, 145-149. <https://doi.org/10.1016/j.tecto.2009.02.010>
- [36] Baratoux, L., Metelka, V., Naba, S., Jessell, M.W., Grégoire, M. and Ganne, J. (2011) Juvenile Paleoproterozoic Crust Evolution during the Eburnean orogeny (2.2-2.0Ga), Western Burkina Faso. *Precambrian Research*, **191**, 18-45. <https://doi.org/10.1016/j.precamres.2011.08.010>
- [37] Ganne, J., Gerbault, M. and Block, S. (2014) Thermo-Mechanical Modeling of Lower Crust Exhumation—Constraints from the Metamorphic Record of the Palaeoproterozoic Eburnean Orogeny, West African Craton. *Precambrian Research*, **243**, 88-109. <https://doi.org/10.1016/j.precamres.2013.12.016>
- [38] Parra-Avila, L.A., Baratoux, L., Eglinger, A., Fiorentini, M.L. and Block, S. (2019)

- The Eburnean Magmatic Evolution across the Baoulé-Mossi Domain: Geodynamic Implications for the West African Craton. *Precambrian Research*, **332**, Article ID: 105392. <https://doi.org/10.1016/j.precamres.2019.105392>
- [39] Grenholm, M., Jessell, M. and Thebaud, N. (2019) Paleoproterozoic Volcano- Sedimentary Series in the ca. 2.27-1.96 Ga Birimian Orogen of the Southeastern West African Craton. *Precambrian Research*, **328**, 161-192. <https://doi.org/10.1016/j.precamres.2019.04.005>
- [40] Bonzi, W.M.E., Lichtervelde, M.V., Vanderhaeghe, O., André-Mayer, A.S., Salvi, S. and Wenmenga, U. (2022) Insights from Mineral Trace Chemistry on the Origin of NYF and Mixed LCT + NYF Pegmatites and Their Mineralization at Mangodara, SW Burkina Faso. *Mineralium Deposita*, **58**, 75-104. <https://doi.org/10.1007/s00126-022-01127-x>
- [41] Bonzi, W.M.E., Vanderhaeghe, O., Lichtervelde, M.V., Wenmenga, U., André-Mayer, A.S., Salvi, S. and Poujol, M. (2021) Petrogenetic Links between Rare Metal-Bearing Pegmatites and TTG Gneisses in the West African Craton: The Mangodara District of SW Burkina Faso. *Precambrian Research*, **364**, Article ID: 106359. <https://doi.org/10.1016/j.precamres.2021.106359>
- [42] Milési, J.P., Feybesse, J.L., Ledru, P., Dommaget, A., Ouédraogo, M.F., Marcoux, E., Prost, A.E., Vinchon, C., Sylvain, J.P., Johan, V., Teguey, M., Calvez, J.Y. and Lagny, P. (1989) Les minéralisations aurifères d'Afrique de l'Ouest. Leurs relations avec l'évolution lithostructurale au Protérozoïque inférieur. *Chroniques Recherche Minière France*, **497**, 3-98.
- [43] Ilboudo, H., Sawadogo, S., Zongo, G.H., Naba, S., Wenmenga, U. and Lombo, M. (2020) Geochemistry and Geodynamic Constraint of Volcanic and Plutonic Magmatism within the Banfora Belt (Burkina-Faso, West-Africa): Contribution to Mineral Exploration. *Geological Society of London*, **502**, 283-307. <https://doi.org/10.1144/SP502-2019-86>
- [44] Ouattara, G. (1998) Structure du Batholite de Ferkessédougou (Secteur de Zuenoula, Côte d'Ivoire). Master's Thesis, Université d'Orléans, Orléans.
- [45] Kretz, R. (1983) Symbols for Rock-Forming Minerals. *American Mineralogist*, **68**, 277-279.
- [46] Janousek, V., Farrow, C.M. and Erban, V. (2006) Interpretation of Whole-Rock Geochemical Data in Igneous Geochemistry: Introducing Geochemical Data Toolkit (GCDkit). *Journal of Petrology*, **47**, 1255-1259. <https://doi.org/10.1093/petrology/egl013>
- [47] Aitchison, J. (1986) The Statistical Analysis of Compositional Data. Chapman and Hall, London.
- [48] Kaiser, H.F. (1960) The Application of Electronic Computers to Factor Analysis. *Educational and Psychological Measurement*, **20**, 141-151. <https://doi.org/10.1177/001316446002000116>
- [49] Pearce, J.A. (1996) Sources and Settings of Granitic Rocks. *Episodes*, **19**, 120-125. <https://doi.org/10.18814/epiiugs/1996/v19i4/005>
- [50] Bonnet, A.L. and Corriveau, L. (2007) Alteration Vectors to Metamorphosed Hydrothermal Systems in Gneissic Terranes. In: Goodfellow, W.D., Ed., *Mineral Deposits of Canada: A Synthesis of Major Deposit-Types, District Metallogeny, the Evolution of Geological Provinces, and Exploration Methods*. Geological Association of Canada, Mineral Deposits Division, Geological Association of Canada, Newfoundland, 1035-1049.
- [51] Corriveau, L. and Spry, P.G. (2014) Metamorphosed Hydrothermal Ore Deposits.

In: Scott, S.D., Ed., *Treatise on Geochemistry (2nd Edition)*, Elsevier, Amsterdam, 175-194. <https://doi.org/10.1016/B978-0-08-095975-7.01107-4>

- [52] Pearce, J.A. and Norry, M.J. (1979) Petrogenetic Implications of Ti, Zr, Y, and Nb Variations in Volcanic Rocks. *Contributions to Mineralogy and Petrology*, **69**, 33-47. <https://doi.org/10.1007/BF00375192>
- [53] MacLean, W.H. and Kranidiotis, P. (1987) Immobile Elements as Monitors of Mass Transfer in Hydrothermal Alteration; Phelps Dodge Massive Sulfide Deposit, Matagami, Quebec. *Economic Geology*, **82**, 951-962. <https://doi.org/10.2113/gsecongeo.82.4.951>
- [54] Trépanier, S., Mathieu, L., Daigneault, R. and Faure, S. (2016) Precursors Predicted by Artificial Neural Networks for Mass Balance Calculations: Quantifying Hydrothermal Alteration in Volcanic Rocks. *Computers and Geosciences*, **89**, 32-43. <https://doi.org/10.1016/j.cageo.2016.01.003>
- [55] Reimann, C., Filzmoser, P. and Garrett, R.G. (2005) Background and Threshold: Critical Comparison of Methods of Determination. *Science of the Total Environment*, **346**, 1-16. <https://doi.org/10.1016/j.scitotenv.2004.11.023>
- [56] Gaillard, N., Williams-Jones, E.A., Clark, J.R., Lypaczewski, P., Salvi, S., Perrouty, S., Piette-Lauzière, N., Guilmette, C. and Linnen, R.L. (2018) Mica Composition as a Vector to Gold Mineralization: Deciphering Hydrothermal and Metamorphic Effects in the Malartic District, Quebec. *Ore Geology Reviews*, **95**, 789-820. <https://doi.org/10.1016/j.oregeorev.2018.02.009>
- [57] Hokka, J. (2020) Geology, Alteration and Lithogeochemistry of the Paleoproterozoic Korpela VMS Occurrence in Eastern Finland. *Mineralium Deposita*, **55**, 1581-1604. <https://doi.org/10.1007/s00126-020-00954-0>
- [58] Xu, K., Xu, D., Deng, T., Li, Z., Zou, S., Wang, Z., Hai, Y., Zhang, S., Qian, Q. and Guo, S. (2022) Genesis of Altered Slate Type Ores in the Huangjindong Gold Deposit, Jiangnan Orogenic Belt, South China. *Journal of Geochemical Exploration*, **241**, Article ID: 107047. <https://doi.org/10.1016/j.jexplo.2022.107047>
- [59] Couture, J.F. and Guha, J. (1990) Relative Timing of Emplacement of an Archean Lode-Gold Deposit in an Amphibolite Terrane: The Eastmain River Deposit, Northern Quebec. *Canadian Journal of Earth Sciences*, **27**, 1621-1636. <https://doi.org/10.1139/e90-172>
- [60] Dubé, B., Mercier-Langevin, P., Kjarsgaard, I., Hannington, M., Béchu, V., Côté, J., Moorhead, J., Legault, M. and Bédard, N. (2014) The Bousquet 2-Dumagami World-Class Archean Au-Rich Volcanogenic Massive Sulfide Deposit, Abitibi, Quebec: Metamorphosed Submarine Advanced Argillic Alteration Footprint and Genesis. *Economic Geology*, **109**, 121-166. <https://doi.org/10.2113/econgeo.109.1.121>
- [61] Detraz, G. and Loubat, H. (1984) Faciès à disthène, staurotide et grenat dans un micaschiste appartenant à l'unité des gneiss du Sapey (Vanoise, Alpes françaises). *Géologie Alpine*, **60**, 5-12.
- [62] Ibarguchi, J.I.G., Mendoza, M. and Girardeau, J. (1991) Mg- and Cr-Rich Staurolite and Cr-Rich Kyanite in High-Pressure. *American Mineralogist*, **76**, 501-511.
- [63] Azambre, B. and Guitard, G. (2001) Disthène et staurotide reliques dans les métapelites du Canigou (Pyrénées orientales). Relations avec les épisodes hercyniens de basses et moyennes pressions. *Earth and Planetary Sciences*, **333**, 601-609. [https://doi.org/10.1016/S1251-8050\(01\)01670-6](https://doi.org/10.1016/S1251-8050(01)01670-6)
- [64] Mathieu, L. (2018) Quantifying Hydrothermal Alteration: A Review of Methods. *Geosciences*, **8**, Article 245. <https://doi.org/10.3390/geosciences8070245>

- [65] Phillips, S.E., Argles, W.T., Warren, J.C., Harris, W.N.B. and Kunz, B.E. (2023) Kyanite Petrogenesis in Migmatites: Resolving Melting and Metamorphic Signatures. *Contributions to Mineralogy and Petrology*, **178**, Article No. 10. <https://doi.org/10.1007/s00410-022-01991-w>
- [66] MacLean, W.H. and Barrett, T.J. (1993) Lithogeochemical Techniques Using Immobile Elements. *Journal of Geochemical Exploration*, **48**, 109-133. [https://doi.org/10.1016/0375-6742\(93\)90002-4](https://doi.org/10.1016/0375-6742(93)90002-4)
- [67] Bierlein, F.P., Arne, D.C., McKnight, S. and Lu, J. (2000) Wall-Rock Petrology and Geochemistry in Alteration Halos Associated with Mesothermal Gold Mineralization, Central Victoria, Australia. *Economic Geology*, **95**, 283-312. <https://doi.org/10.2113/gsecongeo.95.2.283>
- [68] Large, R.R., Gemmell, J.B., Paulick, H. and Huston, D.L. (2001) The Alteration Box Plot: A Simple Approach to Understanding the Relationship between Alteration Mineralogy and Lithogeochemistry Associated with Volcanic-Hosted Massive Sulfide Deposits. *Economic Geology*, **96**, 957-971. <https://doi.org/10.2113/gsecongeo.96.5.957>
- [69] Cail, T.L. and Cline, J.S. (2001) Alteration Associated with Gold Deposition at the Getchell Cartin-Type Gold Deposit, North-Central Nevada. *Economic Geology*, **96**, 1343-1359. <https://doi.org/10.2113/gsecongeo.96.6.1343>